Combinatorial patterns of graded RhoA activation and uniform F-actin depletion promote tissue curvature

Marlis Denk-Lobnig[1], Natalie C Heer[1], Adam C Martin[1, 2]

---

[1] Biology Department, Massachusetts Institute of Technology, 77 Massachusetts Ave., Cambridge, MA 02139

[2] Corresponding author: acmartin@mit.edu

Abstract

During development, gene expression regulates cell mechanics and shape to sculpt tissues. One example is epithelial folding, which proceeds through distinct cell shape changes that occur in different regions of the tissue. How transcription factors combinatorially coordinate cell shape across a tissue is poorly understood. Here, using *Drosophila melanogaster* as a model, we investigate how cell shape changes are coordinated to promote tissue bending during gastrulation. By quantifying the multicellular patterns of RhoA activation, F-actin, and myosin-2 and perturbing RhoA activation, we find that Snail and Twist regulate distinct patterns of graded F-actin accumulation and uniform F-actin depletion, which synergize to create zones of high and low F-actin levels within the *Drosophila* mesoderm. Graded actomyosin results from a gradient in RhoA activation and the width of this zone regulates tissue curvature. Thus, changes in tissue shape are regulated through the choreographed interplay of distinct gene expression patterns.

Introduction

During development, the three-dimensional shape of a complex organism is generated based on patterning that is encoded by the one-dimensional sequence of nucleotides in the genome. Patterns of gene expression, and resulting signaling processes, overlap and interact in space and time to define each cell's function. For example, morphogen gradients encode positional information for specific cell fates (Rogers and Schier, 2011; Wolpert, 1969). For tissues to obtain their final shape and functional state, not only do cell fates need to be positionally specified, but also cell shapes and mechanical properties; mechanical properties and force generation are often patterned within a group of cells of the same fate (Mongera et al., 2018; Sui et al., 2018; Sumigray et al., 2018). Each tissue shape change requires coordinated changes in cell shape and position across the tissue, which have to be tailored to the tissue's morphological and functional requirements while exhibiting robustness and reproducibility between individual embryos/organisms (Chanet et al., 2017; Hong et al., 2016; von Dassow and Davidson, 2009).

Mesoderm invagination in the early *Drosophila melanogaster* embryo is an established model system for gene expression patterning and morphogenesis (Leptin, 2005). This system is powerful to study tissue folding because of its relative simplicity; in this process, a single epithelial sheet at the surface of the embryo folds, driven by geometric shape change of non-dividing cells (i.e., the number of cells is constant). Mesoderm invagination requires apical constriction, a cell shape change driven by actomyosin contraction that converts columnar epithelial cells to a wedge shape and promotes tissue curvature (Leptin and Grunewald, 1990; Sweeton et al., 1991). Importantly, apical constriction is coordinated across the presumptive mesoderm; there is a spatial, ventral-lateral gradient of apical non-muscle Myosin-2 (myosin) and apical constriction that is centered within the mesoderm (Heer et al., 2017; Lim et al., 2017; Spahn and Reuter, 2013) (Figure 1 A). A zone of maximal apical constriction extends from the ventral midline up to 2 cell diameters on each side, while apical constriction beyond cell row 2 gradually declines up to 5 cells from the midline (Heer et al., 2017). At the border of this gradient, about 2 - 4

51 lateral cell rows (row ~ 6 – 9) stretch their apical surface and bend toward the forming furrow
52 (Heer et al., 2017; Leptin and Grunewald, 1990; Sweeton et al., 1991). In contrast, more
53 lateral cells, which are part of the neighboring ectoderm, maintain almost constant apical
54 area throughout the folding process (Rauzi et al., 2015). We investigated how this tissue-
55 wide pattern of cell shape is established and its relevance to achieving proper tissue shape.
56 Mesoderm cell shape change and cell fate are initiated by the transcription factors
57 Twist and Snail, which exhibit distinct patterns of expression (Boulay et al., 1987; Furlong et
58 al., 2001; Leptin, 1991; Thisse et al., 1988). In the early syncytial blastoderm, *twist* mRNA is
59 expressed in a narrow band along the anterior-posterior axis on the ventral side of the
60 embryo, which expands dorsally into a wider band at the cellular blastoderm stage (Leptin,
61 1991). Measurements of the transcription dynamics of Twist target genes, *T48* and *fog*,
62 demonstrate that downstream Twist targets are expressed first at the ventral midline and
63 also expand laterally (Lim et al., 2017). This temporal progression of gene expression results
64 in the graded accumulation of T48 transcripts and protein along the ventral-lateral axis (Heer
65 et al., 2017; Lim et al., 2017; Rahimi et al., 2019). Snail can both activate and repress gene
66 expression (Rembold et al., 2014). One gene that is activated by Snail is the G-protein
67 coupled receptor (GPCR), Mist (Manning et al., 2013). In contrast to graded Twist activity,
68 Snail activity as assessed by Mist mRNA expression is uniform across the mesoderm (Lim et
69 al., 2017). Furthermore, Snail expression exhibits a sharp boundary between mesoderm and
70 ectoderm, whereas Twist expression is graded, extending up to ~2-3 cells across this
71 boundary into the ectoderm (Leptin, 1991). How these overlapping but distinct expression
72 patterns combinatorially contribute to cell shape change across the tissue is not understood.
73 The Twist target gene Fog activates the Mist GPCR and a uniformly expressed
74 GPCR, Smog (Costa et al., 1994; Kerridge et al., 2016; Manning et al., 2013). This GPCR
75 pathway, in parallel with T48 expression, results in apical myosin activation (Kolsch et al.,
76 2007). The GPCR pathway and T48 act via the guanine nucleotide exchange factor (GEF)
77 RhoGEF2, which activates RhoA (Barrett et al., 1997; Hacker and Perrimon, 1998).
78 Functioning in opposition to RhoGEF2 is the RhoA GTPase-activating protein (GAP) C-GAP

(Cumberland-GAP or RhoGAP71E) (Mason et al., 2016). RhoA coordinately activates myosin via Rho-associated and coiled coil kinase (ROCK), and F-actin assembly via the formin Diaphanous (Dawes-Hoang et al., 2005; Homem and Peifer, 2008). Myosin activation occurs in a gradient that is narrower than the mid-cellularization gradient of Twist mRNA accumulation (Heer et al., 2017). How the Twist activity pattern translates to RhoA activation and how RhoA controls the tissue-wide pattern of actomyosin are not known.

During apical constriction, F-actin is apically enriched in ventral cells and proper F-actin organization depends on RhoA signaling (Fox and Peifer, 2007). Conversely, upregulation of F-actin turnover and decreased F-actin levels have been shown in the mesoderm, which allows dynamic actomyosin network reattachment to junctions during constriction (Jodoin et al., 2015). How F-actin is regulated across the mesoderm tissue and how this is associated with patterned myosin and cell shape change are not understood.

Here we show that the tissue-level pattern of F-actin levels is distinct from myosin activation and Twist activity. Snail activity uniformly depletes F-actin across the mesoderm. Graded Twist activity promotes an actomyosin gradient within the zone of F-actin depletion, creating distinct zones of constriction and stretching. We show that the width of this actomyosin gradient is tuned by the activity of the RhoA pathway, which regulates tissue curvature and lumen size in the mesodermal tube structure that results from this fold. Our results show how the combination of overlapping transcriptional pre-patterns coordinates cell shapes across the mesoderm to promote proper tissue curvature.

Results

Myosin and F-actin exhibit distinct tissue-level patterns during mesoderm invagination

Apical myosin activation occurs in a multicellular gradient around the ventral midline (Figure 1 A) (Heer et al., 2017; Lim et al., 2017; Spahn and Reuter, 2013). However, how F-actin is patterned is unknown. To determine the distribution of F-actin levels during mesoderm invagination, we stained embryos with labeled phalloidin and measured cortical F-actin levels by cell row, similarly to how we had measured multicellular patterns of myosin (Heer et al., 2017). This method involved binning cells at different positions from the ventral midline in order to obtain an average protein signal per cell at a given position along the ventral-lateral axis. In contrast to myosin, for which the activated pool accumulates at the apical surface, F-actin (as detected by phalloidin) is most apparent at intercellular junctions. Junctional F-actin levels were higher in the ectoderm than the neighboring mesoderm cells during ventral furrow formation (Jodoin et al., 2015). The difference in F-actin levels between mesoderm and ectoderm was already present before ventral furrow initiation: there was a clear boundary between low (mesoderm) and high (ectoderm) F-actin concentration zones starting at mid-late cellularization, before apical constriction had started (Figure 1 B and D and Supplement to Figure 1 A). During ventral furrow formation, junctional F-actin at the center of the mesoderm increased to form a gradient that extended from cell 2 to cell 6, similar to apical myosin (Figure 1 C and D).

The result of F-actin accumulation in ventral midline cells and persistent F-actin depletion in marginal mesoderm cells was a zone of junctional F-actin depletion in cell rows ~ 6 - 9 of the mesoderm and a discrete boundary between mesoderm and ectoderm (Figure 1C), forming a pattern distinct from that of myosin (Figure 1A). This pattern was also observed in live embryos expressing the actin-binding domain of utrophin fused to green fluorescent protein (Utrophin::GFP) or mCherry (Utrophin::mCherry), but not with a general

125 membrane marker, Gap43-mCherry, indicating that this measurement is not a fixation
126 artifact or due to changes in plasma membrane structure (Supplement to Figure 1 B). The
127 lower levels of F-actin were not as striking in Utrophin::GFP as in phalloidin-stained
128 embryos, likely because Utrophin interferes with F-actin remodeling (Spracklen et al., 2014);
129 however, we were able to reproducibly detect differences between mesoderm and ectoderm.

130 The observed tissue-wide pattern of F-actin was strikingly similar to the pattern of
131 apical constriction and stretching. Cell rows that maintained low F-actin levels were the
132 same cell rows at the margin of the mesoderm that stretched during folding (Figure 1 A, C).
133 This led us to hypothesize that F-actin levels could influence cell mechanics and the ability to
134 stretch under stress, which has been shown in other contexts (Salbreux et al., 2012; Stricker
135 et al., 2010). To test the strength of this relationship, we plotted the average cell junctional F-
136 actin intensity as a function of apical cell area for both mesoderm and adjacent ectoderm
137 cells (Figure 1 E). We found that F-actin levels were anti-correlated with cross-sectional
138 apical area. In summary, unlike apical myosin, junctional F-actin exhibited a clear difference
139 between mesoderm and ectoderm, which could explain why lateral mesoderm cells stretch
140 while neighboring ectoderm cells maintain their apical area during tissue folding.

141

142 **Snail and Twist regulate distinct components of the F-actin pattern**

143 To determine whether patterned gene expression regulates F-actin across the mesoderm,
144 we tested how the transcription factors *snail* and *twist* affect the tissue-level pattern of F-
145 actin levels. Snail activity in the mesoderm, as measured by *mist* transcription, is uniform
146 (Lim et al., 2017). We found that the Snail expression boundary co-localized precisely with
147 the boundary in F-actin depletion (Figure 2 A). Therefore, Snail expression and cortical F-
148 actin depletion are correlated.

149 Next, we determined whether cortical F-actin depletion is dependent on *snail.* Unlike
150 control (heterozygous) embryos, *snail* homozygous mutant embryos expressing
151 Utrophin::GFP did not exhibit patterned cortical F-actin levels in the ventral region (Figure 2
152 B). Quantification of subapical F-actin levels across the ventral and ventral-lateral domain in
153 *snail* mutants revealed no boundary, but uniform intensity throughout the region (Figure 2 C).
154 In addition, *snail* mutants lacked the ventral gradient in F-actin accumulation, consistent with
155 Snail being required for downstream effects of Twist, such as apical myosin activation and
156 dynamics (Kolsch et al., 2007; Martin et al., 2009). Because *snail* mutant embryos were
157 imaged live, we were able to confirm that we were examining ventral cells based on
158 germband extension movements in the neighboring ectoderm and premature cell divisions
159 that occurred in the uninternalized mesoderm, which is mitotic domain 10 (Foe, 1989;
160 Grosshans and Wieschaus, 2000). Therefore, Snail promotes uniform F-actin depletion
161 across mesoderm cells prior to gastrulation.

162 In contrast to Snail, the pattern of Twist activity across the mesoderm temporally
163 evolves, with Twist targets initiating first along the ventral midline and then expanding
164 laterally, which results in a gradient of accumulated transcripts (Lim et al., 2017; Rahimi et
165 al., 2019). To determine the effects of *twist,* we examined F-actin levels in a *twist* null mutant
166 that has been shown to disrupt myosin stabilization (Martin et al., 2009). In contrast to *snail*
167 mutants, *twist* mutant embryos exhibited F-actin depletion in the mesoderm and a clear
168 boundary to more lateral tissue with higher F-actin levels (Figure 2 D, E). The zone of F-actin
169 depletion was decreased to about half the normal width, consistent with previous studies
170 showing that *twist* mutants reduce the width of *snail* expression (Leptin, 1991). However,
171 graded F-actin accumulation around the ventral midline was absent in *twist* mutants,
172 suggesting that it specifically depends on the Twist pathway, which includes RhoA
173 activation. Therefore, mesodermal control of F-actin by Twist and Snail is comprised of two
174 nested layers: 1) prior to ventral furrow formation, uniform Snail activity depletes F-actin
175 across the mesoderm, and 2) during ventral furrow formation, graded Twist activity increases

176 F-actin accumulation in a ventral-lateral gradient (similar to apical myosin), but marginal
177 mesoderm cells maintain lower cortical F-actin.

178

179 **RhoA activation occurs in a gradient**

180 We next investigated how the gradient in Twist activity is transduced into a gradient of
181 actomyosin. Fog and T48 transcripts accumulate in a gradient (Lim et al., 2017; Rahimi et
182 al., 2019), but how downstream RhoA activation is patterned was not known. Fluorescently
183 tagged versions of RhoA's activator RhoGEF2 (under an endogenous promoter, Figure 3 B),
184 the Anillin Rho-binding domain, an active RhoA sensor (Figure 3 D), and the RhoA effector
185 ROCK (Figure 3 F) became apically enriched in ventral cells during ventral furrow formation,
186 consistent with previous studies (Kolsch et al., 2007; Mason et al., 2013; Mason et al.,
187 2016). Quantification of apical fluorescence by cell row revealed that all three markers for
188 RhoA pathway activation were graded along the ventral-lateral axis, exhibiting strong
189 fluorescence at the ventral midline and gradually decreasing to baseline after 5 cells (Figure
190 3 C, E, and G). In contrast, endogenously tagged C-GAP-GFP was largely cytoplasmic and
191 appeared uniform across the ventral domain during folding (Supplement to Figure 3 A).

192 The width of the gradient in RhoA activation, about 5 cells from the ventral midline, is
193 narrower than that of Twist mRNA, which extends 10-12 cells from the ventral midline (Heer
194 et al., 2017). Thus, RhoA activation occurs in a gradient, but the gradient does not mirror
195 Twist activity, suggesting that additional factors may modulate the downstream activity of the
196 Twist pathway.

197

198 **Neither graded myosin activation nor F-actin depletion depend on intercellular**
199 **mechanical connections**

200 Our data suggests that Snail and Twist promote uniform mesodermal F-actin depletion prior
201 to apical constriction and subsequent graded actomyosin activation within the mesoderm
202 during furrow formation, respectively. In the ventral furrow and the related process of
203 *Drosophila* posterior midgut formation, it has been proposed that mechanical feedback
204 between constricting cells is required to induce myosin accumulation, which may contribute
205 to a gradient or wave in contractility (Bailles et al., 2019; Mitrossilis et al., 2017). Therefore, it
206 was possible that mechanical induction of myosin also contributes to the gradient.

207 To determine the contributions of mechanical induction to multicellular patterns of
208 myosin activation and cortical F-actin levels, we examined embryos in which intercellular
209 cytoskeletal coupling was disrupted. We did this by depleting the adherens junction protein
210 α-catenin by RNA interference (α-catenin-RNAi). α-catenin-RNAi has been shown to
211 dramatically uncouple the cytoskeletal meshworks of cells from the junctions and disrupt the
212 formation of supracellular structures in the mesoderm (Figure 4 A, Supplemental Movies S1,
213 2) (Fernandez-Gonzalez and Zallen, 2011; Martin et al., 2010; Yevick et al., 2019). In α-
214 catenin-RNAi embryos, ventral cell apical area remains at pre-gastrulation levels (about 40
215 μm^2), but myosin contracts into spot-like structures at the apical cell surface (Figure 4 A , B,
216 E) (Martin et al., 2010). Quantification showed that, despite the lack of mechanical coupling,
217 active myosin reproducibly accumulated in a gradient around the ventral midline (Figure 4 C,
218 E). Therefore, graded myosin activation across the tissue does not depend on force
219 transmission between cells. However, the shape of the gradient appeared less sigmoidal in
220 α-catenin-RNAi, suggesting that mechanical feedback could affect gradient shape.

221 We then asked whether mesodermal F-actin depletion depends on intact adherens
222 junctions. Adherens junctions are a known target of Snail in the mesoderm (Chanet and
223 Schweisguth, 2012; Dawes-Hoang et al., 2005; Kolsch et al., 2007) and adherens junction
224 components exhibit a similar tissue-level pattern to F-actin (Supplement to Figure 4A). We
225 examined F-actin by staining α-catenin-RNAi embryos with phalloidin. Similar to wild-type
226 embryos, F-actin in α-catenin-RNAi embryos was depleted across the mesoderm with a

227 sharp boundary to the ectoderm before the start of contractile behavior (Figure 4 D, E). This
228 suggested that F-actin regulation by Snail does not depend on intact junctions. Depletion in
229 lateral mesoderm cells was maintained over time despite a lack of stretching in those cells.
230 Interestingly, junctional F-actin levels around the midline did not appear to be increased the
231 same as in wild-type embryos during constriction. However, medio-apical F-actin foci
232 appeared, which co-localized with myosin, presumably because actomyosin was uncoupled
233 from intercellular junctions (Supplement to Figure 4 B). These results indicated that F-actin
234 depletion in the mesoderm does not require intact adherens junctions and is not caused by
235 cell stretching.

236

237 **RhoA activation level modulates actomyosin gradient width within F-actin depleted**
238 **zone**

239 The above results suggested a Twist activity gradient leads to a RhoA activation gradient.
240 However, the gradient in Twist mRNA and accumulated T48 transcripts extends beyond the
241 5-6 cell rows from the ventral midline where we detect RhoA activation (Heer et al., 2017;
242 Lim et al., 2017; Rahimi et al., 2019). Therefore, we hypothesized that the gradient in Twist
243 activity is not simply transmitted, but is shaped by the signaling network downstream of
244 Twist. Mesodermal RhoA signaling involves a signaling circuit, which includes an
245 activator/inhibitor pair (Figure 3A). The activator RhoGEF2 is required for high levels of
246 apical myosin accumulation (Dawes-Hoang et al., 2005; Nikolaidou and Barrett, 2004). The
247 inhibitor, C-GAP, has been shown to disrupt proper subcellular myosin localization when
248 severely depleted in ventral cells (Mason et al., 2016). To test the importance of this circuit in
249 regulating the coordination of contractility, we quantified actomyosin contractility in embryos
250 where either C-GAP or RhoGEF2 levels were tuned to an extent that did not fully disrupt
251 subcellular myosin localization, but did change tissue-wide patterning.

252 First, we examined apical, activated myosin after elevating net RhoA activation by
253 either depleting C-GAP by RNAi (C-GAP-RNAi) or overexpressing RhoGEF2 (RhoGEF2
254 O/E). These perturbations elevated myosin in mesoderm cells, but did not elevate
255 contractility in the ectoderm at this stage (Figure 5 A). C-GAP-RNAi does not prevent basal
256 myosin loss in mesoderm cells (Mason et al., 2016), suggesting that this perturbation
257 specifically affects contractility on the apical side. In control embryos, apical myosin is
258 activated within 5 cells from the ventral midline. In contrast, C-GAP-RNAi and RhoGEF2 O/E
259 extended myosin activation to 7-8 cells away from the midline, with 3-4 cells on each side of
260 the ventral midline having uniformly high myosin intensity (Figure 5 B). C-GAP-RNAi also
261 extended the width of RhoA activation as detected by the active RhoA sensor (Supplement
262 to Figure 5 A). Consistent with the expansion of contractility, measurements of apical area
263 demonstrated that C-GAP-RNAi and RhoGEF2 O/E resulted in a wider zone of uniform
264 apical constriction, which changed from 2 cells on either side of midline up to 4 cells on each
265 side (Figure 5 C). Thus, our data suggested that increasing RhoA activation through C-GAP
266 depletion or RhoGEF2 overexpression widens the activated myosin gradient.

267 Next, we examined how increasing RhoA activation affected the F-actin pattern. We
268 found that, similar to its effect on myosin, increased net RhoA activation expanded the zone
269 of higher F-actin levels around the ventral midline, which is consistent with RhoA regulating
270 actin (Fox and Peifer, 2007). The increased width of F-actin elevation resulted in a narrower
271 region of depleted F-actin (Figure 5 D) without changing the position of the mesoderm-
272 ectoderm boundary (Supplement to Figure 5 B). In some cases, RhoGEF2 O/E completely
273 eliminated the pattern of F-actin depletion and elevation across the mesoderm during folding
274 (Figure 5 D), presumably because ventral F-actin accumulation expanded to the whole
275 mesoderm. In contrast, RhoGEF2 depletion resulted in a wider region of depleted F-actin
276 (Figure 5 E). Of note, RhoGEF2 depletion decreased the density of myosin-accumulating
277 cells and overall myosin levels, but did not visibly narrow the myosin gradient (Supplement
278 to Figure 5 C), suggesting that F-actin and myosin induction might be differently sensitive to

279 RhoA levels in our experimental setup. By quantifying the number of cell rows with depleted
280 F-actin, we found that the width of F-actin depletion appears inversely related to net RhoA
281 activation (Figure 5 F). Thus, the level of RhoA activation set by the GEF/GAP balance
282 determines the width of the F-actin gradient within the larger zone of F-actin depletion.

283

284 **Myosin pulses elicit different area responses in midline versus margin mesoderm**
285 **cells**

286 So far, we focused on the patterns of average intensity and area in cell rows at a single
287 timepoint; however, myosin contractility in the ventral furrow is highly dynamic and exhibits
288 pulses (Martin et al., 2009). Myosin pulses are discrete events in which there is a burst of
289 myosin accumulation and often constriction of the cell apex. RhoA activity levels determine
290 the contractile outcome of a myosin pulse in individual cells (Mason et al., 2016). Given that
291 RhoA activity is graded across the furrow (Figure 3), we examined the behavior of myosin
292 pulses throughout the mesoderm. There are distinct classes of myosin pulses that are
293 known to occur in constricting cells during furrow formation. 'Ratcheted pulses' are events
294 where apical, active myosin persists after a pulse and decreased apical area is sustained
295 (Figure 6 A). In contrast, 'unratcheted pulses' exhibit myosin dissipation after the pulse and
296 exhibit cell relaxation. There is a continuum of behaviors from ratcheted to unratcheted,
297 which are associated with high and low RhoA activity, respectively (Mason et al., 2016).
298 Myosin pulse behavior in stretching cells is not well understood.

299 To determine whether the ventral-lateral gradient in RhoA patterns myosin pulse
300 type, we examined myosin persistence across different cell rows. Consistent with previous
301 measurements of contractile pulses in the middle of the ventral furrow (Xie and Martin,
302 2015), pulses close to the ventral midline exhibited persistent myosin; the myosin level after
303 the pulse was higher than the baseline before the pulse (Figure 6 B, cell row 1). Myosin
304 persistence was associated with a sustained decrease in apical area (Figure 6 C, cell row 1)

305 (Xie and Martin, 2015). In contrast, myosin pulses in more lateral mesoderm cells (Figure
306 6C, cell row 4) did not exhibit strong myosin persistence (Figure 6 B, cell row 7). These
307 myosin pulses were associated with area constriction, but cells partially relaxed after each
308 pulse. In marginal mesoderm cells (Figure 6C, cell row 7), myosin pulses still occurred, but
309 exhibited even less persistence. These myosin pulses accompanied cell stretching and did
310 not robustly result in cell apex constriction (Figure 6 C, cell row 7). Comparing pulse
311 behavior across different ventral-lateral positions, we found a graded decrease in myosin
312 persistence and area stabilization after pulses with distance from the ventral midline (Figure
313 6D), with marginal cells increasing their area during myosin pulses.

314 To confirm the differences in myosin pulses that we observed by determining the
315 average pulse behavior, we examined the cross-correlation between the constriction rate
316 (positive for apical area decrease) and the rate of myosin density change in cells along the
317 ventral-lateral axis, independently of pulse detection. Consistent with cell apical constriction
318 occurring during a myosin pulse, cells closest to the ventral midline exhibited a strong
319 positive correlation (Figure 6 E). Peak correlation decreased gradually up to 5 cells from the
320 ventral midline (Figure 6 E). Cells ~7-8 rows from the midline, in which apical area increases
321 during a myosin pulse (Figure 6 C), exhibited a negative correlation, indicating that these
322 cells with lower F-actin levels (Figure 1) stretch specifically when myosin increases (Figure 6
323 F). This behavior was specific to mesoderm cells at this stage because ectoderm cells did
324 not exhibit either a positive or negative correlation (Figure 6 G, cell rows 11, 12). Thus, there
325 are different myosin pulse behaviors depending on ventral-lateral position in the mesoderm.

326

327 **The actomyosin gradient width regulates furrow curvature and lumen size**

328 To examine the role of the wild-type contractile pattern in ventral furrow formation, we tested
329 how disrupting this pattern affected tissue shape. In wild-type embryos with graded
330 constriction, the ventral furrow is a sharp, v-shaped fold with high curvature at its center

331 (Figure 7A). Previous work showed that globally changing cell fate to create a much wider
332 mesoderm and contractile domain lowered the curvature of the furrow (Heer et al., 2017).
333 However, these experiments disrupted cell fate across the entire embryo. Here, we
334 investigated the role of the actomyosin gradient in folding, independently of cell fate. Upon
335 identifying C-GAP, we had found that some C-GAP-RNAi embryos have a more C-shaped,
336 less sharp fold (Mason et al., 2016). Therefore, we directly tested how widening the gradient
337 with C-GAP-RNAi or RhoGEF2 O/E affected the curvature of the ventral furrow. C-GAP-
338 RNAi and RhoGEF2 O/E embryos with a wider myosin gradient often had lower central
339 curvature than in wild-type (Figure 7 B and C, Supplement to Figure 7A and B). However,
340 the RhoGEF2 O/E phenotype was variable and the mean curvature was not significantly
341 different from control embryos (Figure 7 B and C, Supplement to Figure 7A and B). Most
342 embryos with low central curvature still fold successfully, although in some extreme cases
343 the mesoderm was not internalized. Successful folding in C-GAP-RNAi and RhoGEF2 O/E
344 embryos was associated with a significantly enlarged lumen when invaginated mesoderm
345 formed a tube (Fig. 7C).

346 Conversely, decreased RhoA activation in RhoGEF2-RNAi caused higher central
347 curvature (Supplement to Figure 7A, B). Although these embryos appeared to fold
348 successfully, in some cases, cells at the embryo surface, around the ventral midline,
349 underwent cell division immediately after invagination (Supplemental Movies S3,4). Because
350 the mesoderm is mitotic domain 10 (Foe, 1989), this suggests that a narrower band of
351 mesoderm invaginated and that some marginal mesoderm cells were left outside.

352 To explore the relationship between the contractile pattern and fold curvature further,
353 we tested whether the contractile pattern of an individual embryo is correlated with tissue
354 curvature in that embryo at a later time during folding. We segmented and binned cells from
355 12 live-imaged embryos (4 per genotype) to obtain their tissue-wide myosin and constriction
356 patterns. The same embryos were subsequently followed to measure cross-sectional tissue
357 curvature (averaged across three points along the anterior-posterior axis) at about 10 μm

358 invagination depth during folding and lumen size after folding. Linear regression analysis
359 revealed that the half-maximal gradient width was inversely correlated with curvature (Figure
360 7D). Consistent with the actomyosin gradient width determining the number of F-actin
361 depleted cell rows, the number of F-actin depleted cell rows was also correlated with
362 curvature in a separate experiment (Supplement to Figure 7C). Thus, gradient width and the
363 number of F-actin depleted cell rows are defining factors of the curvature of the ventral
364 furrow.

365 **Discussion**

366 Here, we showed that tissue folding is coordinated by cell shape changes across the tissue
367 that emerge from the combination of overlapping transcription factor and signaling patterns
368 (Figure 7 E). First, we found that there is a Snail-mediated uniform decrease in cortical F-
369 actin levels across the mesoderm. This decrease persists in cells at the lateral margin of the
370 mesoderm, with a sharp boundary to higher F-actin-containing ectoderm cells. Second, we
371 found that Twist activity that is refined by RhoA regulation gives rise to a gradient of
372 actomyosin. We showed that RhoA activation occurs in a tissue-level gradient and that
373 modulating the balance of RhoGEF2 to C-GAP shifts the width of this gradient. Importantly,
374 the levels and dynamics of myosin and F-actin in distinct cell groups are correlated with their
375 shape changes, leading us to speculate that differences in F-actin density and myosin
376 persistence between cell groups determine apical constriction vs. stretching behavior across
377 the ventral domain (Figure 7 E).

378 **Snail-mediated uniform mesodermal F-actin depletion**

379 We observed that during folding, cells with high F-actin levels tend to maintain their shape or
380 constrict, whereas low-F-actin cells stretch. The role of F-actin cortex density in a cell's
381 response to mechanical stress is well documented (Stricker et al., 2010). In the marginal
382 mesoderm, lower cortical F-actin levels in stretching cells is compounded by lower levels of
383 zonula adherens proteins (Dawes-Hoang et al., 2005; Kolsch et al., 2007; Weng and
384 Wieschaus, 2016), both of which could promote the ability of these cells to remodel and
385 stretch in response to stress. In contrast, the neighboring ectoderm and the medial ventral
386 cells have high F-actin and adherens junction density, which may help those cells maintain
387 their shape or even constrict under stress. Importantly, the effect of Snail on F-actin is
388 independent of functional adherens junction assembly, suggesting that Snail targets several
389 cellular processes in parallel to promote mesoderm cell remodeling.

390 Alternatively, it was possible that cell strain/stretching or constriction contributed to
391 decreased F-actin density (Latorre et al., 2018). However, the fact that F-actin depletion
392 occurs before stretching and is not disrupted when cells are prevented from constricting and
393 stretching their neighbors suggests that F-actin depletion is not driven by cell shape change.
394 In fact, the transcription factor Snail appears to uniformly deplete F-actin prior to cell shape
395 change. The mechanism by which Snail decreases F-actin is unknown and will be an area of
396 future study. Snail could possibly regulate F-actin assembly via Diaphanous or Enabled (Fox
397 and Peifer, 2007; Homem and Peifer, 2008), or F-actin disassembly via regulation of Cofilin
398 (Jodoin et al., 2015).

399 **Twist and RhoA signaling create an actomyosin gradient within the Snail domain**

400 Nested within this zone of Snail mediated F-actin depletion, Twist activity causes
401 actomyosin accumulation via graded RhoA activation. This combination of two overlapping
402 transcription patterns allows for domains of different cell behaviors and mechanical
403 properties within a tissue of uniform cell fate (mesoderm). We further found that patterning of
404 constricting and stretching domains is tightly regulated by the RhoA regulators RhoGEF2
405 and C-GAP; disrupting that pattern even slightly causes changes to the shape of the
406 resulting fold. RhoGTPases are regulated by complex interactions between their (activating)
407 GEFs and (inhibiting) GAPs in many contexts (Denk-Lobnig and Martin, 2019); in the ventral
408 furrow specifically, interactions between C-GAP and RhoGEF2 tune sub-cellular localization
409 and dynamics of the contractile apparatus during folding (Mason et al., 2016). Here, we
410 found that small changes to C-GAP or RhoGEF2 levels, which do not strongly disrupt cell-
411 level organization, change the pattern of actomyosin levels across the ventral domain.
412 Specifically, this property is dependent on the ratio of RhoGEF2 and C-GAP, or net RhoA
413 activation: C-GAP RNAi and RhoGEF2 O/E both widen the domain of high actomyosin, and
414 create a uniform high-contractility domain around the ventral midline. Conversely, RhoGEF2
415 RNAi narrows the F-actin gradient and furrow, and creates a wider domain of F-actin-
416 depleted cells.

417 Our data suggests a system with a graded activator (RhoGEF2) and a uniform
418 inhibitor (C-GAP), in which the inhibitor buffers overall activation and creates an activation
419 threshold (Figure 7 E). We propose that the activation threshold regulates the width of the
420 actomyosin gradient: the gradient widens if overall activator levels increase or inhibitor levels
421 decrease; it narrows if the activator level is decreased. A widened central region of uniform
422 contractility can emerge if some part of the system is saturated at sufficient RhoA activation
423 levels, consistent with our measurements of the contractile gradient in RhoGEF2 O/E and C-
424 GAP-RNAi embryos. If RhoA activation is decreased, such as in RhoGEF2 RNAi embryos,
425 this mechanistic model predicts a narrower gradient. This appears to be true for the F-actin
426 pattern.

427 Myosin levels in RhoGEF2-RNAi were decreased overall and fewer cells
428 accumulated myosin, but the myosin gradient width was the same as in wild-type. F-actin
429 and myosin may respond to low RhoA activity because they have different thresholds for
430 accumulation, possibly because they are controlled by different regulators downstream of
431 RhoA or. In addition, expression of fluorescently tagged Utrophin actin-binding domain,
432 which disrupts F-actin dynamics (Spracklen et al., 2014), appears to interact with RhoA
433 disruptions, amplifying the phenotype of high RhoA activation and reducing the cell-level
434 effects of RhoGEF2 RNAi. This is consistent with the notion that RhoA activation promotes
435 F-actin assembly across the tissue.

436 A prediction of this model is that the upstream activator RhoGEF2 should be graded
437 over a wider region in wild-type than the downstream myosin. Our measurements of
438 RhoGEF2::GFP show a gradient of similar width as myosin, however the small signal-to-
439 noise ratio of the RhoGEF2::GFP probe could obscure the lateral tails of that gradient. The
440 upstream *twist* mRNA and T48 protein gradient is several cells wider than the myosin
441 gradient (Heer et al., 2017), consistent with a possibly wider activation gradient of RhoGEF2.

442 Our data show that the gradient shape is tuned by a RhoA activator-inhibitor pair.
443 There are other points in the pathway where balance between inhibition and activation is
444 likely to contribute to tissue-wide patterning. In particular, GPRK2, an inhibitor of GPCR
445 signaling, affects myosin organization and cell behaviors (Fuse et al., 2013; Jha et al., 2018).
446 In GPRK2 mutant embryos, apical constriction is expanded, such that lateral mesoderm cells
447 that normally stretch accumulate myosin and constrict (Fuse et al., 2013). This is consistent
448 with a potential role for GPRK2 restricting the contractile gradient. Further downstream,
449 myosin activity is regulated directly by the balance of ROCK and myosin phosphatase
450 (Munjal et al., 2015; Vasquez et al., 2014) and several actin regulators tune the balance of
451 F-actin assembly and disassembly in ventral furrow formation (Fox and Peifer, 2007;
452 Homem and Peifer, 2008; Jodoin et al., 2015). Control of tissue-wide properties by
453 overlapping patterns of regulators, such as F-actin regulation by Snail and Twist and
454 actomyosin gradient regulation by C-GAP and RhoGEF2, appears to be a powerful
455 mechanism to create complex spatial patterns of cell behavior.

456 **Fold curvature is tuned by tissue-wide actomyosin patterning**

457 Our disruptions of the actomyosin gradient demonstrate that tissue curvature is
458 sensitive to tissue-wide contractile patterns. The width and position of the contractile
459 gradient is important for the shape of the resulting fold. We showed that adjusting the width
460 of actomyosin gradient by modulating the levels of RhoGEF2 or C-GAP influences tissue
461 curvature. Elevating RhoA activity creates a wider gradient and results in C-shaped furrows
462 with low curvature. By using inherent patterning variability in wild-type and extended
463 variability in genetic disruptions, we showed that the contractile pattern of an individual
464 embryo is correlated with subsequent folding and post-fold shape, suggesting that it would
465 be possible to partially predict tissue curvature based on the observed myosin pattern of an
466 embryo. This is consistent with past work suggesting that broadening contractility lowers
467 tissue curvature. For example, depletion of the ventral fate inhibitor, Serpin27A, caused a
468 wider mesoderm, to form an abnormally shallow furrow (Heer et al., 2017). Similarly, in

469 GPRK2 mutants, which do not affect the width of the mesoderm, all cells within the
470 mesoderm (~18 cells) constrict and create a U-shaped furrow that often fails to close (Fuse
471 et al., 2013). How F-actin patterning is affected in either of those cases is not known.

472 That increased contractility in the tissue decreases fold curvature may seem counter-
473 intuitive, but computational modeling shows that graded contractility creates a sharper fold
474 than uniformly high contractility (Heer et al. 2017). Force balance between neighboring high-
475 contractility cells prevents efficient constriction in the uniform case, whereas in the graded
476 case, central high-contractility cells can constrict efficiently against their lower-contractility
477 neighbors, causing a sharp hinge. Considering that successful constriction of cells is
478 dependent on the mechanics of their neighbors, it is plausible that the stretching lateral
479 mesoderm domain can further promote higher curvature folds (Ko et al., 2020; Perez-
480 Mockus et al., 2017; Sui et al., 2018). While we were not able to specifically change F-actin
481 levels because of pleiotropic effects of modulating F-actin dynamics (Jodoin et al., 2015), we
482 speculate that changes to the width of the “soft”, F-actin depleted domain, concomitant with
483 changing gradient width, likely contributed to our observed folding phenotypes. Ventral
484 furrow formation is an embryo-wide mechanical process: it depends on embryo shape
485 (Chanet et al., 2017) and relates to cell shape changes on the opposite, dorsal side of the
486 embryo (Rauzi et al., 2015). Our results further emphasize the importance of understanding
487 tissue-wide mechanics during folding.

488 Development generates a multitude of tissue curvatures in different contexts. We
489 showed that folding is sensitive to small patterning changes of actomyosin. Our discovery
490 suggests a mechanism by which actomyosin and mechanical cell properties might be
491 patterned in other tissues to generate distinct curvatures.

492

493 **Materials and Methods**

494 **Fly stocks and crosses**

495 For a list of fly stocks and crosses used in this study, see Supplemental Table S1.

496 An N-terminal GFP tag was inserted at the endogenous C-GAP locus using CRISPR-
497 Cas9 as previously described (Gratz et al., 2015). Coding sequences for two 15 base pair
498 (bp) gRNAs targeting neighboring sites 5' of the *rhoGAP71E* gene start codon were cloned
499 into the pU6-BbsI plasmid using the CRISPR Optimal Target Finder (Gratz et al., 2014; Iseli
500 et al., 2007). The donor template plasmid for homology directed repair was generated using
501 Exponential Megapriming PCR (Ulrich et al., 2012). A plasmid backbone (from pHD scarless
502 DS Red) containing an ampicillin resistance gene and an origin of replication was combined
503 with two homology arms (1219 bp and 1119bp, respectively) homologous to the region
504 around the *rhoGAP71E* gene start codon, flanking a *GFP* encoding DNA sequence (kindly
505 provided by Iain Cheeseman) with an N-terminal 4 amino acid-encoding linker region (Ser-
506 Gly-Gly-Ser). Both plasmids were injected into nanos>Cas9 expressing embryos. Surviving
507 adults were crossed to y,w; +;+ flies and then screened for mosaic GFP insertion by PCR.
508 Progeny of GFP-positive injected flies were crossed to y,w;+;Dr/TM3 flies and then screened
509 by PCR for the GFP insertion. Successful insertions were further analyzed by sequencing.
510 The fly stock established from their offspring was later back-crossed once to OreR flies in
511 order to eliminate potential off-target mutations. Homozygous C-GAP-GFP flies were viable,
512 suggesting that the GFP-tagged C-GAP is functional.

513 **Live and fixed imaging**

514 Embryos were prepared for live imaging as previously described (Martin et al., 2009).
515 Embryos were collected in plastic cups covered with apple-juice plates. Flies were allowed to
516 lay eggs for 2–4 h at 25 °C (or temperature as noted in Table S1). The plate was removed
517 and the embryos immersed in Halocarbon 27 oil for staging. Embryos undergoing

518 cellularization were collected. Embryos were dechorionated with 50% bleach, washed with
519 water, and then mounted on a slide with embryo glue (Scotch tape resuspended in heptane),
520 with the ventral side facing upwards. A chamber was made with two no. 1.5 coverslips as
521 spacers and was filled with Halocarbon 27 oil for imaging. Images were acquired on a Zeiss
522 710 microscope with an Apochromat 40×/1.2 numerical aperture W Korr M27 objective.
523 Channels were excited and detected concurrently.
524 Immuno- and phalloidin staining was performed using standard methods (Martin et
525 al., 2009). Embryos were fixed with 8% paraformaldehyde in PO_4 buffer and heptane (3:4)
526 for 30 min, devitellinized manually, stained with phalloidin, primary antibodies and
527 appropriate fluorescently tagged secondary antibodies, and mounted in AquaPolymount
528 (Polysciences, Inc.). Anti-snail (rabbit, 1:100; formaldehyde-hand peeled fixation; gift from M.
529 Biggin), anti-armadillo (mouse, 1:500; heat-methanol fixation; DSHB), anti-GFP (rabbit,
530 1:500; formaldehyde-hand peeled fixation; Abcam, ab290) and anti-E-cadherin (rat, 1:50;
531 formaldehyde-hand peeled fixation; DHSB) antibodies and AlexaFluor568 phalloidin
532 (Invitrogen) were used. All imaging was carried out on a Zeiss 710 confocal microscope with
533 a Plan-Apochromat 40×/1.2 numerical aperture W Korr M27 objective. Channels were
534 excited and detected concurrently.
535 For imaging settings for each fluorescent marker, refer to Supplemental table S2.

536

537 **Gradient analysis**

538 Analysis was done as described in Heer et al., 2017. All image analysis was performed
539 in Fiji (http://fiji.sc) (Schindelin et al., 2012) and MATLAB (MathWorks). Custom software for
540 image processing is available upon request.

541

542 **1) Definition of developmental timing**

543 Wild-type embryos were staged based on time of folding. The accuracy of this method
544 was confirmed by comparing constricted areas per bin at the selected time point. For
545 embryos with disrupted constriction and folding, a time point was chosen relative to the
546 beginning of myosin/ fluorescence accumulation.

547

548 **2) Shell projection and thresholding to measure apical fluorescence intensity**

549 Shell projections of the apical surface were conducted as previously described (Heer et
550 al., 2017). First, cytoplasmic background signal (defined as the mean cytoplasmic signal plus
551 2.5 standard deviations) was subtracted from the myosin channel (Martin et al., 2009;
552 Vasquez et al., 2014). For non-myosin fluorescent signal (Figure 3), the cytoplasmic
553 background subtraction was adjusted to account for differences in signal-to-noise ratio for
554 different fluorescent markers (RhoGEF2::GFP: mean + 2 standard deviations (SDs);
555 aniRBD::GFP: mean + 2 SDs , rok::GFP: mean + 2.5 to 3 SDs, GFP::C-GAP: no background
556 subtraction).

557 The maximum myosin (or other apically enriched fluorescent) signal intensity in the *z*-
558 plane was used to generate a rough map of the embryo surface. A Fourier transform was
559 used to generate a smooth continuous surface. Myosin signal was averaged over the 4 μm
560 above the surface and membrane signal was the sum of the signal from 1-2 μm below the
561 surface. A gaussian blur filter (radius 1 pixel for fluorescent signal, 0.7-1 membranes) was
562 applied after shell projection to reduce noise.

563 Shell projections from live and immunostained images were then segmented using
564 an existing MATLAB package, Embryo Development Geometry Explorer (EDGE) (Gelbart et
565 al., 2012). Membrane signal (Gap43::mCherry) or cortical F-actin (phalloidin or Utr::GFP)
566 projections were used to detect cell boundaries (and track cells for live images). Myosin (or
567 equivalent signal) shell projection was used to measure apical signal accumulation.

568 Segmentation errors in were corrected manually. Our segmentation algorithm was used to
569 determine centroid position, cell diameter, cell area, cell perimeter as well as total
570 myosin/fluorescence signal per cell.

571

572 **3) Cell bins**

573 For all image quantification, data was segregated into 'cell bins' i.e. cell rows relative to the
574 ventral midline (Heer et al. 2017). Cells were assigned to bins based on the ventral-lateral
575 position of the cell centroid. The ventral midline was defined as the position at which the
576 furrow closes. In fixed images or for embryos that did not fold (or rotated while folding), the
577 position of the VM was determined by symmetry of the fluorescent signal and constriction.
578 Live images were binned based on initial position of the cell centroid before tissue
579 contraction and folding and the boundaries of the bins were set by the average cell diameter
580 along the ventral-lateral axis. For images in which cells had already begun to constrict, the
581 width of each bin was set manually (but still relative to average cell diameter) to approximate
582 the width of cells at that ventral-lateral position. We used MATLAB to generate box-and-
583 whiskers plots depicting the distribution of data, overlaid with the mean of each bin. For
584 boxplots, bottom and top sides of the box represent 25th and 75th percentile of cells,
585 respectively. Outliers were defined as values 1.5 times bigger than the interquartile range.
586 Fluorescent signal was normalized by dividing by the mean of the first bin to adjust for
587 variability in imaging conditions.

588 **Cortical F-actin quantification**

589 For apical projections of phalloidin staining (Figure 1A, 2A and 4B), embryos were
590 shell-projected and cells tracked the same way as for myosin and other markers (see
591 above), except that no background subtraction was applied. To measure cortical F-actin
592 intensity, we integrated the signal intensity of pixels within 2 μm of the identified cell

593 boundaries . This total junctional F-actin signal was divided by the cell perimeter to obtain
594 junctional F-actin density.

595 Because mesodermal F-actin depletion was most obvious subapically, not apically,
596 with Utrophin::GFP markers in live embryos (Figures 2B, 5C and 7C), those movies were
597 "shell-projected" in Fiji by generating a Z-reslice (1 μm per slice) and then creating a second
598 reslice along a manually drawn subapical line that followed the ventral-lateral curvature of
599 the embryo surface at about 10-15 μm below the apical surface (Supplement to Figure 2).
600 This allowed us to correct for specific ventral-lateral curvature and get a subapical projection
601 of constant z-depth from the embryo surface. The center part along the anterior-posterior
602 (AP) axis of the shell-projection, where AP curvature is small, was used to quantify F-actin
603 (Utrophin::mCH or ::GFP) intensity along the ventral-lateral axis. We used the FIJI "Plot
604 profile" command, averaging intensity across the AP length of the selection (consistent
605 between embryos) for each pixel row. Intensity profiles were exported, aligned based on
606 position of the ventral midline, smoothed with moving average smoothing (window-size 20)
607 and plotted in Matlab R2019a. Fluorescence signal was normalized by subtracting the mean
608 intensity, to adjust for variability in imaging conditions.

609 Cell rows depleted of F-actin (Figure 5D, Supplement to Figure 5C) were counted
610 manually on the subapicalprojections used for intensity profiles. If depleted regions on both
611 sides of an embryo were visible, both were counted and the average used. Differences in
612 depleted cell rows between genotypes were represented in a box plot using Matlab and
613 statistically compared using the non-parametric two sample Kolmogorov–Smirnov test.

614 **Pulsing analysis**

615 Images of live embryos with myosin and membrane markers during folding were
616 obtained as above, but with faster scan speed and smaller z-depth, to obtain time intervals
617 of 9 to 11 seconds between stacks, which is sufficient to capture typical myosin and area
618 pulsing behavior (Martin et al., 2009). Cells across the mesoderm were tracked over time

619 using EDGE, and cell area and myosin intensity were exported. Using Matlab 2019a, we
620 detected peaks within individual cells of maximal myosin intensity increase, smoothing with a
621 moving average filter and then detecting local maxima. The cell behavior about 100 seconds
622 before and after each maximum was saved as a trace. Pulse traces were averaged for each
623 cell bin to identify average dynamics based on cell position. Persistence of myosin pulses
624 was defined as the minimum myosin intensity within each trace after a peak minus minimum
625 myosin intensity before the same peak. Persistence of area constriction was defined as the
626 maximum cell area after a myosin peak minus maximum cell area before the same peak.
627 Each trace was normalized to the center of the pulse. Persistence values were averaged by
628 bin and plotted in Matlab for an individual embryo.

629 To analyze further the relationship between area and myosin behaviors, we cross-
630 correlated rates of myosin and area change (as described in Martin et al., 2009). We used
631 the xcorr function in Matlab to cross-correlate the change in myosin intensity (myosin
632 intensity at a timepoint minus myosin intensity at the previous time point) with constriction
633 change (cell area at a timepoint minus cell area at the next time point, i.e. cross- positive
634 value if constricting, negative if stretching) for each cell trace. Cross-correlations for each
635 cell were averaged by bin (distance from the midline) and plotted.

636 **Curvature analysis**

637 Movies of the embryos for which we had measured the multicellular myosin gradient
638 (see above) (with at least 20 μm z-depth) were resliced in FIJI to create 1 μm thick cross
639 section images of the ventral furrow at the middle of the AP axis of the embryo. Apically
640 enriched myosin signal was used to trace the surface of the folding tissue with the freehand
641 line tool in Fiji. The fold was traced for a cross section at the center of the AP axis of the
642 embryo as well as for cross-sections 20μm anterior and posterior, respectively. The
643 timepoint of measurement was chosen as when the invagination depth was ~ 10 μm. The
644 XY coordinates of each trace were imported into Matlab R2019a. After manually determining

645 the position of the ventral midline, a circle fit (Nikolai Chernov (2020). Circle Fit (Taubin
646 method)https://www.mathworks.com/matlabcentral/fileexchange/22678-circle-fit-taubin-
647 method), MATLAB Central File Exchange. Retrieved February 5, 2020) was applied to the
648 central part of the trace, 2.5 μm width around the midline. The inverse of the fitted circle
649 radius was defined as the fold curvature. The three traces taken at different AP positions
650 were averaged to obtain the fold curvature value for the embryo. Local curvature as
651 displayed in Figure 7 A and B was generated using LineCurvature2D (Dirk-Jan Kroon
652 (2020). 2D Line Curvature and
653 Normals (https://www.mathworks.com/matlabcentral/fileexchange/32696-2d-line-curvature-
654 and-normals), MATLAB Central File Exchange. Retrieved March 16, 2020.) in Matlab.
655 Post-fold lumen sizes were measured from central cross-sections of the same
656 embryos whose curvature had been analysed, for a single AP position. Lumen area was
657 measured by manually fitting an ellipse to the lumen in each cross-section in Fiji and
658 measuring its area.

659 Curvature and lumen measurements were compared between genotypes using the non-
660 parametric two sample Kolmogorov–Smirnov test.

661 **Regression analysis**

662 All linear regression fits (Figures 1C, 7D, S7C) were performed in Matlab R2019a
663 using the fitlm command. The original data as well as the best fit line were plotted and the R-
664 squared value and best fit slope were reported.

665 For myosin gradients, the position of the most lateral bin with myosin levels above
666 the half-maximal myosin intensity was used to define gradient width. This bin position was
667 then compared to central curvature measurements of the same embryo at a later timepoint
668 (at ~10 μm invagination depth, analyzed with circlefit). For Utrophin::GFP embryos, cell rows
669 with depleted F-actin were counted manually and compared to central curvature of the same
670 embryo at a later timepoint (at ~10 μm invagination depth).

673 **Acknowledgments**

674 We thank N. Perrimon, L. Perkins and the Transgenic RNAi Project at Harvard Medical School
675 (National Institutes of Health/National Institutes of General Medical Sciences R01-GM084947) for
676 providing transgenic RNAi stocks. We thank V. Tserunyan for the software adapted and used
677 here to analyze myosin pulses. We thank B. Adhikary for help with analyses of F-actin levels. We
678 thank current and former Martin lab members for helpful discussions and feedback. This work
679 was supported in part by the NIH Pre-Doctoral Training Grant T32GM007287. Research reported
680 in this publication was supported by the National Institute of General Medical Sciences of the NIH
681 under award number R01GM125646 to A.C.M.

682 **Figure legends**

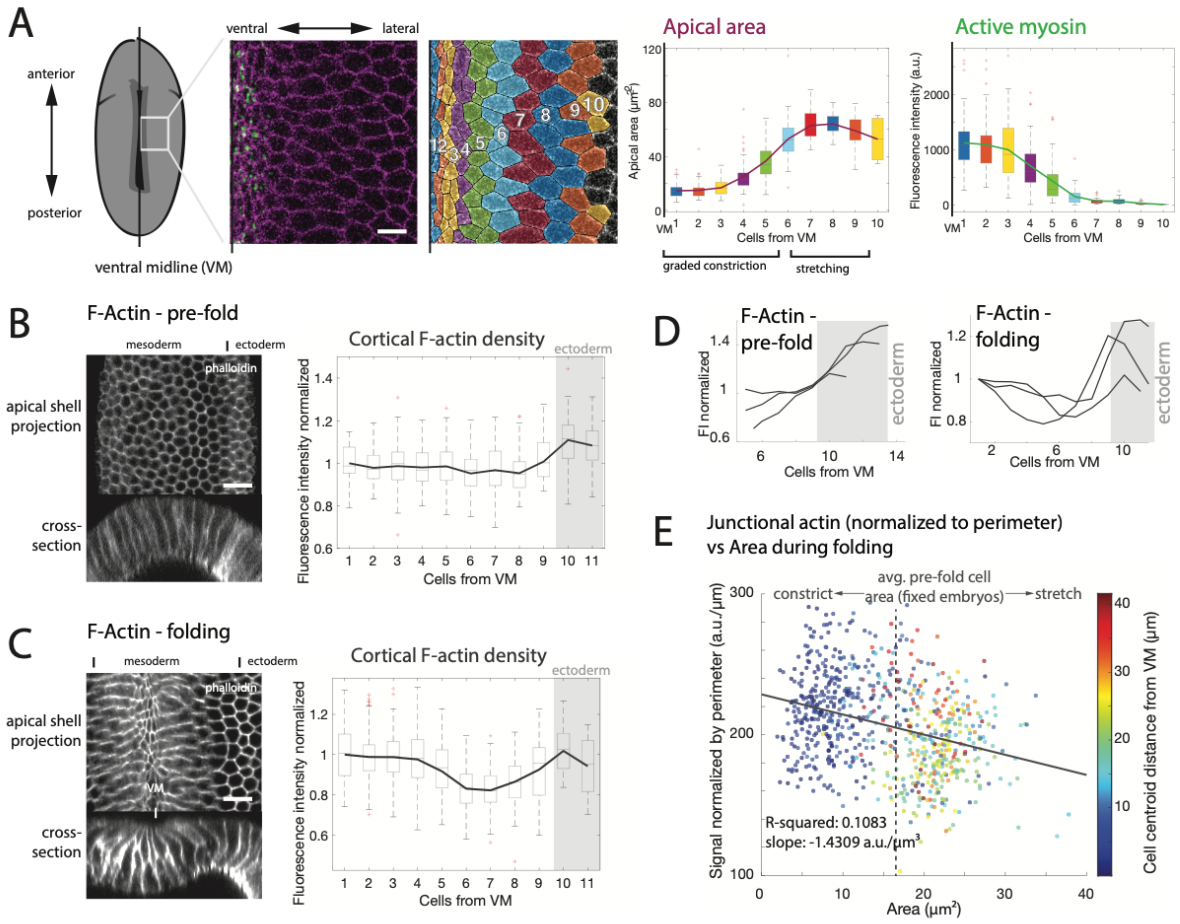

683
684

685 **Figure 1.** Tissue-wide mesodermal F-actin distribution is distinct from Myosin. (**A**) Myosin
686 gradient extends 6 cells from the ventral midline (VM) and remains low. Images are apical
687 surface view of embryo labeled with sqh::GFP (Myosin) and Gap43::mCherry (membrane)
688 and segmented example of embryo with cell rows highlighted in different colors. Scale bar =
689 10 μm. Colors in image correspond to bins in adjacent plots; showing Myosin and apical
690 area distributions in a representative wild-type embryo . Data is represented by box-and-
691 whisker plot, where bottom and top sides of the box represent 25th and 75th percentile of
692 cells, respectively. Midline is the median and red '+' are outliers. Box-and-whisker plot is
693 shown for one representative embryo (corresponds to image on left) with at least 4 cells per
694 bin analyzed (median 52.5 cells). (**B**) Left: F-actin is depleted at the mesoderm-ectoderm

border. Images are apical shell projection (top) or cross-section (bottom) images of phalloidin stained embryos imaged before furrow formation. Scale bar = 10 μm. Right: Plot showing F-actin depletion in the mesoderm. Mean cortical F-actin intensity was calculated from segmented cells. Cortical F-actin density was calculated by integrating F-actin intensity around the cell periphery and dividing by cell perimeter. Cortical F-actin density was normalized to mean of first cell row. Data is represented by box-and-whisker plot, where bottom and top sides of the box represent 25th and 75th percentile of cells, respectively. Midline is the median and red '+' are outliers. Box-and-whisker plot is shown for one representative embryo (corresponds to image on left) with at least 23 cells per bin analyzed (median 52 cells). (**C**) Left: F-actin accumulates in a gradient across the ventral mesoderm. Images are apical shell projection (top) or cross-section (bottom) images of phalloidin stained embryos imaged during furrow formation. Scale bar = 10 μm. Right: Plot showing F-actin depletion in the mesoderm. Mean cortical F-actin intensity was calculated and data represented the same as (B). Box-and-whisker plot is shown for one representative embryo (corresponds to image on left) with at least 15 cells per bin analyzed (median 73 cells). (**D**) Mean F-actin density traces for 3 embryos corresponding to (B) (pre-fold F-actin) and (C) (F-actin during folding), normalized by mean of 9th and 1st cell row, respectively. (**E**) Apical area is inversely correlated with cortical F-actin levels. Quantification of cortical F-actin density per cell (cortical F-actin intensity divided by perimeter) for the embryo shown in (C) was plotted as a function of apical area. Color of data points represents physical distance from ventral midline in μm. Average pre-fold cell area for fixed embryos (~16 μm^2 due to shrinkage during the fixation process) is indicated with dotted grey line. Note that cells towards the margin of the mesoderm have the largest area and lowest F-actin and cells farther out (i.e., ectoderm) have an area centered at ~16 μm^2 and higher F-actin levels.

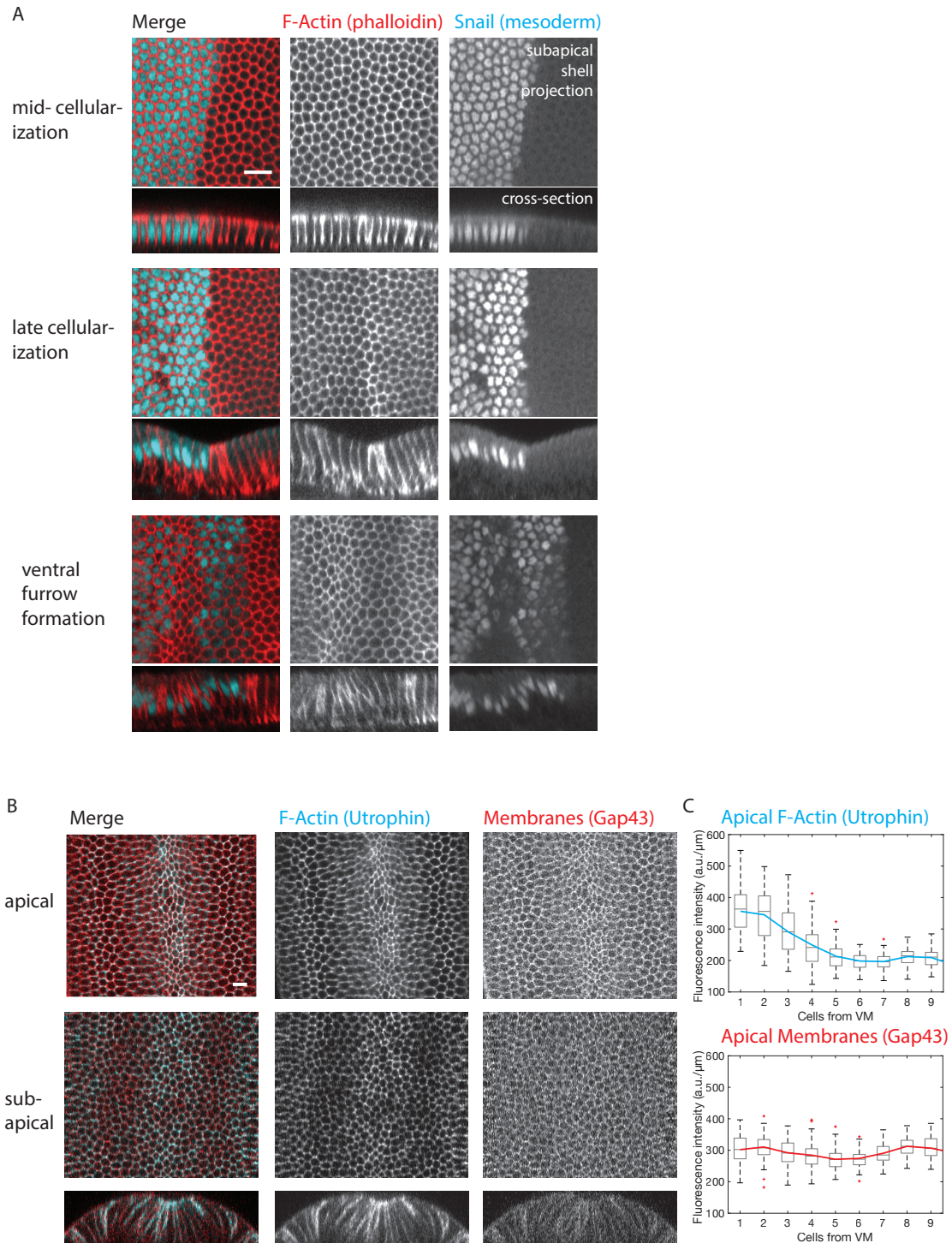

Supplement to Figure 1. F-actin is depleted in the mesoderm during cellularization. (**A**) F-actin depletion in the mesoderm is not present in early cellularization, but appears towards the end of cellularization. Images are subapical shell projections (top) and cross-sections (bottom) of wild-type embryos at different stages stained with phalloidin (red) and anti-snail antibody (cyan). Scale bar = 10 µm. Bending of tissue during late cellularization in cross-

725 section is a fixation artefact. (**B**) F-actin marked by the fluorescently marked Utrophin::GFP
726 (cyan) is depleted in the marginal mesoderm, but a general membrane marker,
727 Gap43::mCherry (red), is not. Images show both markers in apical (top) and subapical
728 (middle) shell projections and cross-sections. Scale bar = 10 μm. (**C**) Quantification by bin of
729 apical Utrophin::GFP (top) and Gap43::mCherry (bottom) junctional fluorescent intensity,
730 divided by perimeter. Although less pronounced, apical Utrophin::GFP shows a similar
731 pattern to phalloidin, with low F-actin density in lateral mesoderm cells compared to
732 ectoderm cells. Data is represented by box-and-whisker plots where each bin is a cell row at
733 a given distance from the ventral midline (at least 67 cells per row analyzed, median 72
734 cells). Bottom and top sides of the box represent 25th and 75th percentile junctional intensity
735 per cell, respectively. Midline is the median and red '+' are outliers.
736

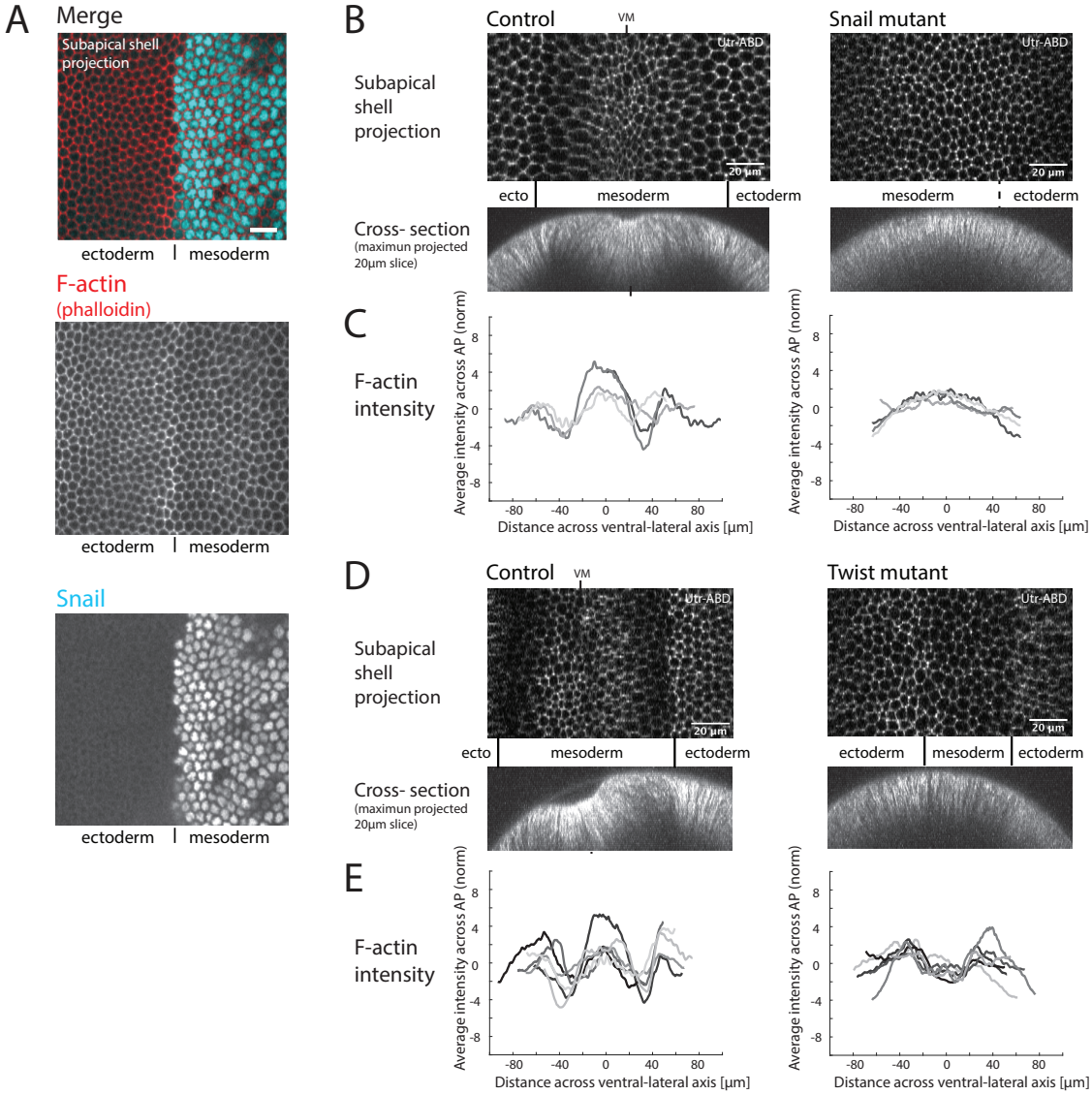

Figure 2. Snail and Twist distinctly regulate the tissue-wide F-actin distribution. (**A**) Snail expression boundary corresponds to F-actin depletion boundary. Images are from phalloidin-stained embryo co-stained with anti-Snail. Scale bar = 10 µm. (**B**) The *snail* mutant disrupts mesodermal F-actin depletion. Images are from representative, live homozygous *snail* mutant and normal sibling embryo expressing Utrophin::GFP (F-actin). The *snail* mutant shows a lack of F-actin patterning. Scale bar = 20 µm. (**C**) Quantification of tissue-wide F-actin intensity profiles from 4 *snail* mutant and 4 normal sibling embryos (See Methods and Supplement to Figure 2). All *snail* mutants lack F-actin patterning. The decreased F-actin intensity at the edges of the ventral-lateral axis reflects the curvature of the tissue, which

747 causes more tissue to scatter light between objective and more lateral parts of the projected
748 layers. (**D**) The *twist* mutant exhibits F-actin depletion, but lacks F-actin elevation around
749 midline. Images are from 6 representative, live homozygous *twist* mutant and 6 normal
750 sibling embryos expressing Utrophin::GFP (F-actin). The *twist* mutant exhibits F-actin
751 depletion. Scale bar = 20 μm. (**E**) Quantification of tissue-wide F-actin intensity profiles from
752 multiple *twist* mutant and normal sibling embryos. All *twist* mutants exhibit F-actin depletion,
753 but not the increase around the midline.

754

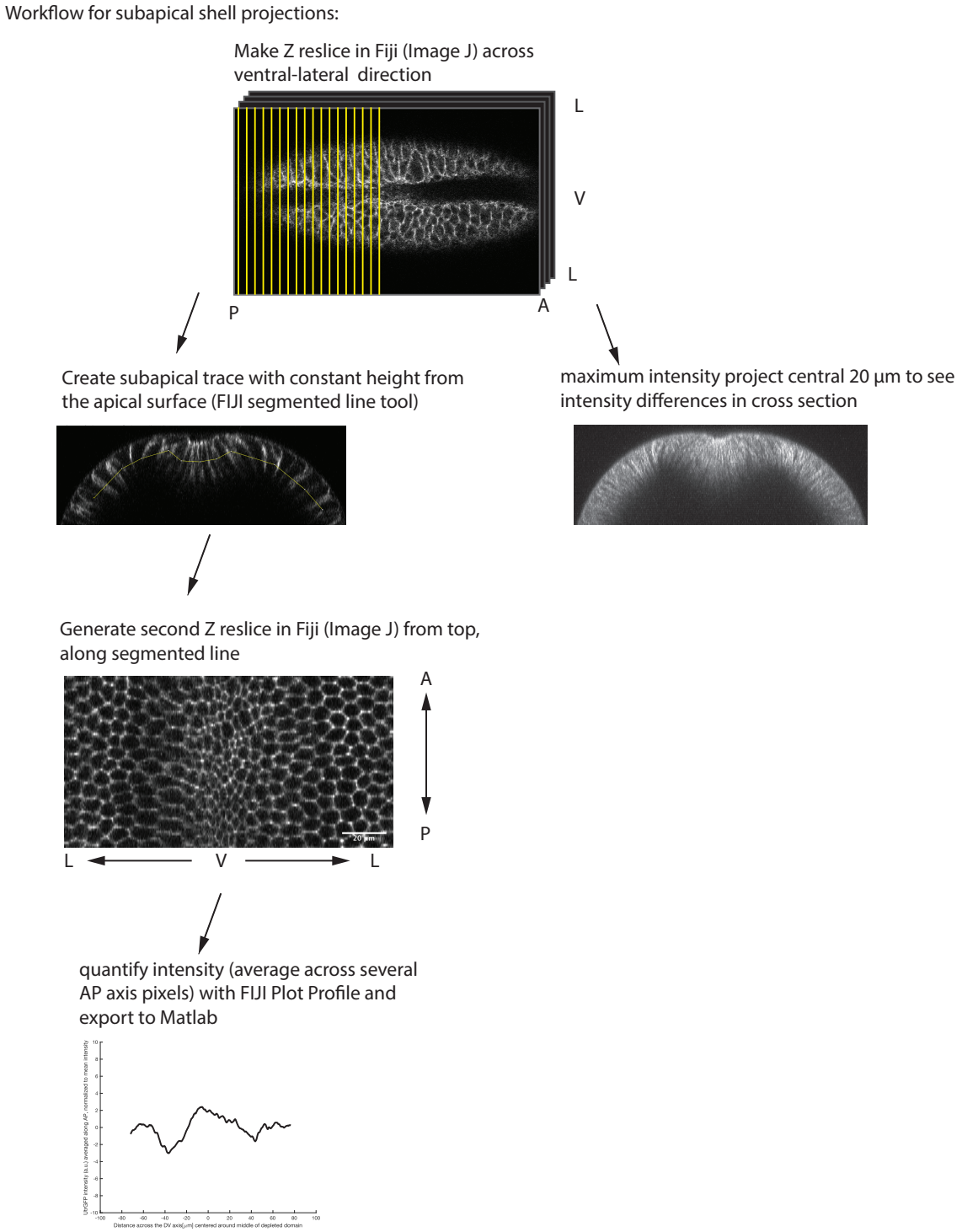

Supplement to Figure 2. Workflow for subapical shell projections in FIJI. Confocal image stacks are resliced along the ventral-lateral axis to get a cross-sectional view. A subapical trace is then drawn manually about 10-15 µm below the apical surface and the embryo is

759 resliced a second time along the trace. The central part of the embryo along the AP axis is

760 then used to quantify intensity along the ventral-lateral axis.

761

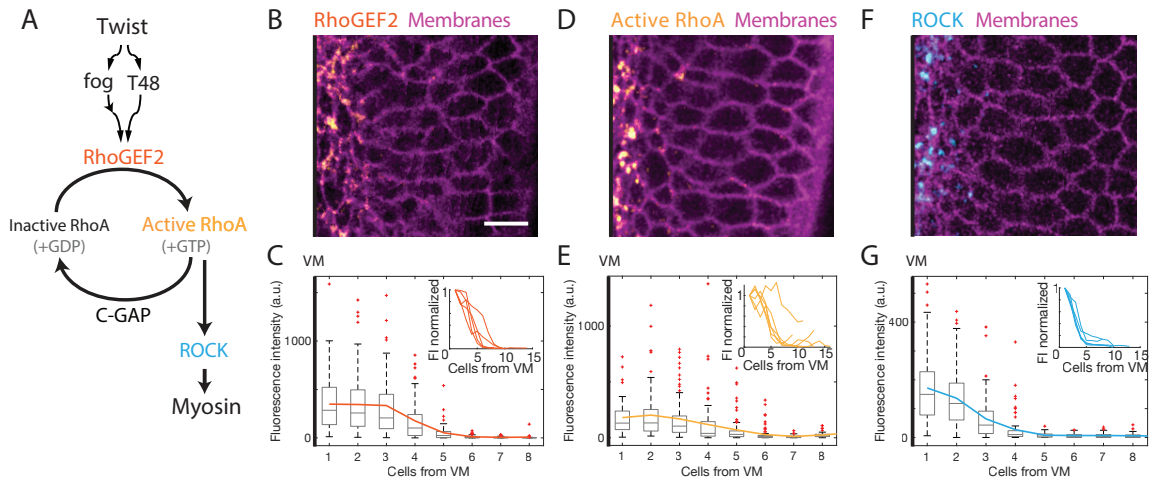

762

763 **Figure 3.** RhoA activation occurs in a gradient. (**A**) Simplified diagram of signaling

764 downstream of Twist, focused on RhoA regulation. (**B**) Image of RhoGEF2::GFP (orange)

765 and Gap43::mCherry (magenta). Ventral midline on left. Scale bar = 10 μm. (**D**) Image of

766 Anillin Rho-binding domain::GFP (yellow) and Gap43::mCherry (magenta). Ventral midline

767 on left. (**F**) Image of Rok::GFP (cyan) and Gap43::mCherry (magenta). Ventral midline on

768 left. (**C, E, G**) Apical RhoGEF2::GFP intensity (orange, **C**), Anillin Rho-binding domain::GFP

769 intensity (yellow, **E**), and Rok::GFP intensity (cyan, **G**) as a function of distance from the

770 ventral midline for one representative embryo, respectively. Data is represented by box-and-

771 whisker plots where each bin is a cell row at a given distance from the ventral midline.

772 Bottom and top sides of the box represent 25th and 75th percentile, respectively. Midline is

773 the median and red points are outliers. At least 32 cells (RhoGEF2, median 85 cells), 58

774 cells (Active RhoA, median 76.5 cells), or 51 cells (ROCK, median 68.5 cells) were analyzed

775 for each cell row, respectively. Insets shows average cell behavior from 5 embryos per

776 condition.

777

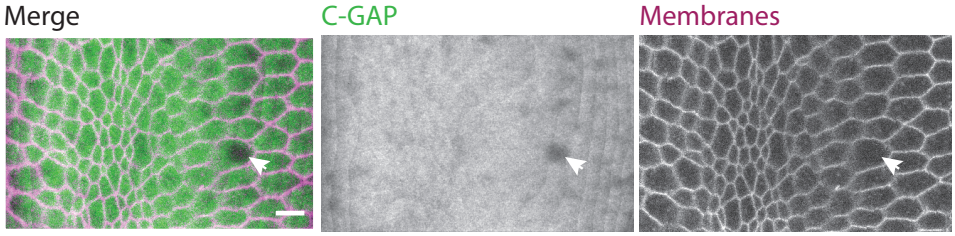

Supplement to Figure 3. C-GAP is uniformly cytoplasmic across the ventral furrow. Apical shell projection of an embryo expressing GFP::C-GAP (green) and gap43::mCherry (membranes, magenta). White arrow indicates apical nucleus with no GFP::C-GAP signal. Scale bar = 10 μm.

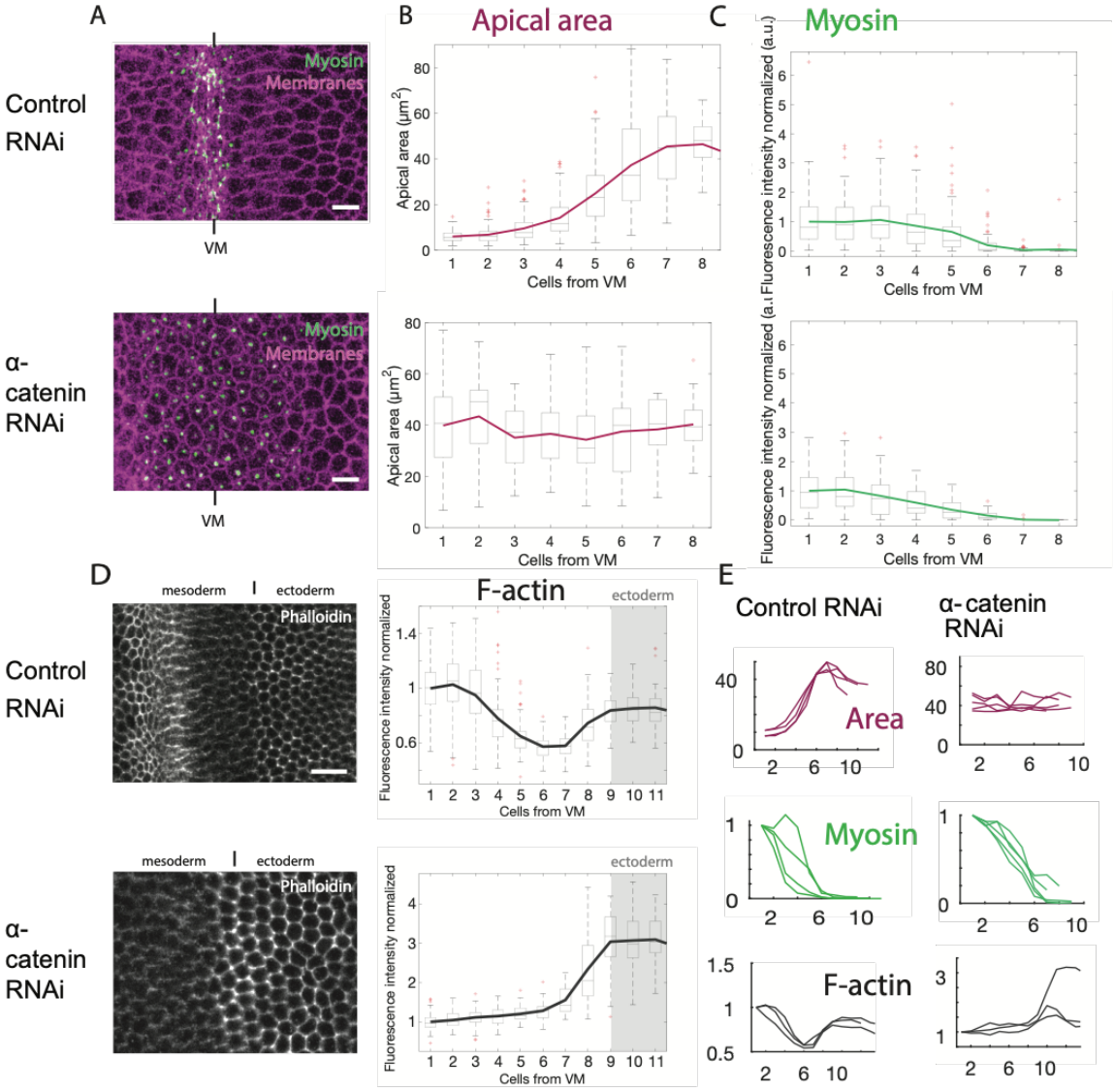

Figure 4. Myosin gradient and uniform F-actin depletion do not require intercellular coupling. (**A**) Images (apical shell projections) of control (Rh3-RNAi) and α-catenin-RNAi embryos expressing sqh::GFP (Myosin, green) and Gap43::mCherry (Membranes, magenta). Scale bar = 10 μm. (**B**) and (**C**) Quantification of apical area (magenta, **B**) and normalized apical, active myosin (green, **C**) as a function of distance from ventral midline. Data is represented by box-and-whisker plots where each bin is a cell row at a given distance from the ventral midline (at least 41 (control) or 44 (α-catenin-RNAi) cells per row analyzed, respectively; median 72 (control) or 107 (α-catenin-RNAi) cells). Bottom and top sides of the box represent 25th and 75th percentile, respectively. Midline is the median and red points are

794 outliers. (**D**) Left: Images of phalloidin-stained control (Rh3-RNAi, top) and α-catenin-RNAi
795 (bottom) embryos focused on the mesoderm-ectoderm boundary. Scale bar = 10 μm. Right:
796 Quantification of normalized cortical F-actin levels in rows of cells along the ventral-lateral
797 axis (at least 52 (control) or 8 (α-catenin-RNAi) cells per row analyzed, respectively; median
798 78 (control) or 40.5 (α-catenin-RNAi) cells). Data is represented by box-and-whisker plots
799 where each bin is a cell row at a given distance from the ventral midline. Bottom and top
800 sides of the box represent 25th and 75th percentile, respectively. Midline is the median and
801 red points are outliers. (**E**) Individual mean traces for multiple control and α-catenin-RNAi
802 embryos. Top: Average apical area behavior from 4 (control) and 5 (and α-catenin-RNAi)
803 different embryos, respectively. Mid: Average active myosin behavior from 4 (control) and 5
804 (and α-catenin-RNAi) different embryos, respectively. Bottom: Average cortical actin
805 behavior from 3 different embryos, respectively
806

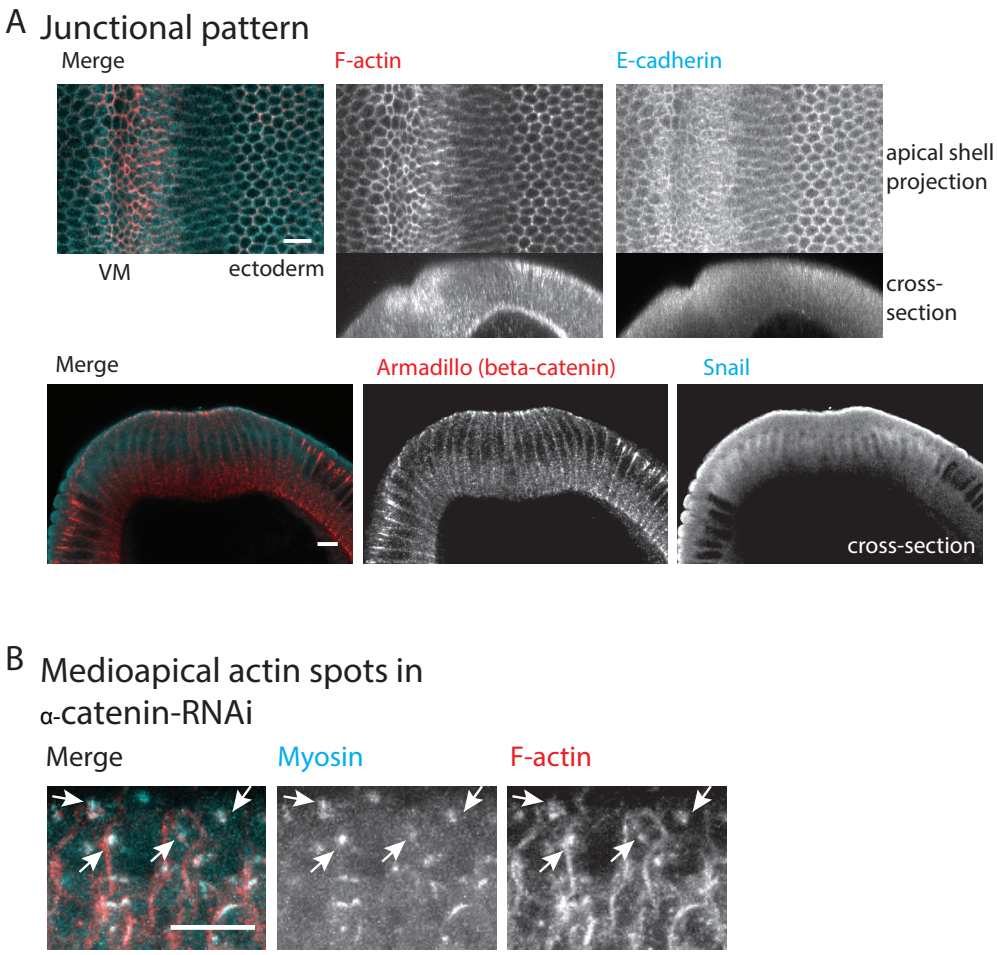

Supplement to Figure 4: F-actin is colocalized with junctions in wild-type and with medioapical myosin spots in α -catenin-RNAi embryos. (**A**) Top: Apical shell projection and cross-section (maximum intensity projection of 20 µm) images of fixed control (Rh3-RNAi) embryo stained with phalloidin (red) and anti-E-cadherin antibody (cyan). Bottom: Cross-section images of control (Rh3-RNAi) embryo stained with anti-armadillo (ß-catenin) antibody (red) and anti-Snail antibody (cyan, marking the mesoderm). Note that transition from low to high F-actin at ectoderm boundary matches adherens junction intensity transition. Scale bars = 10 µm. (**B**) Images of ventral apical surface of fixed embryo expressing sqh::GFP (Myosin light chain marker), stained with phalloidin (red) and anti-GFP (cyan) antibody. White arrows indicate medioapical spots in which myosin and F-actin are colocalized. Scale bar = 10 µm.

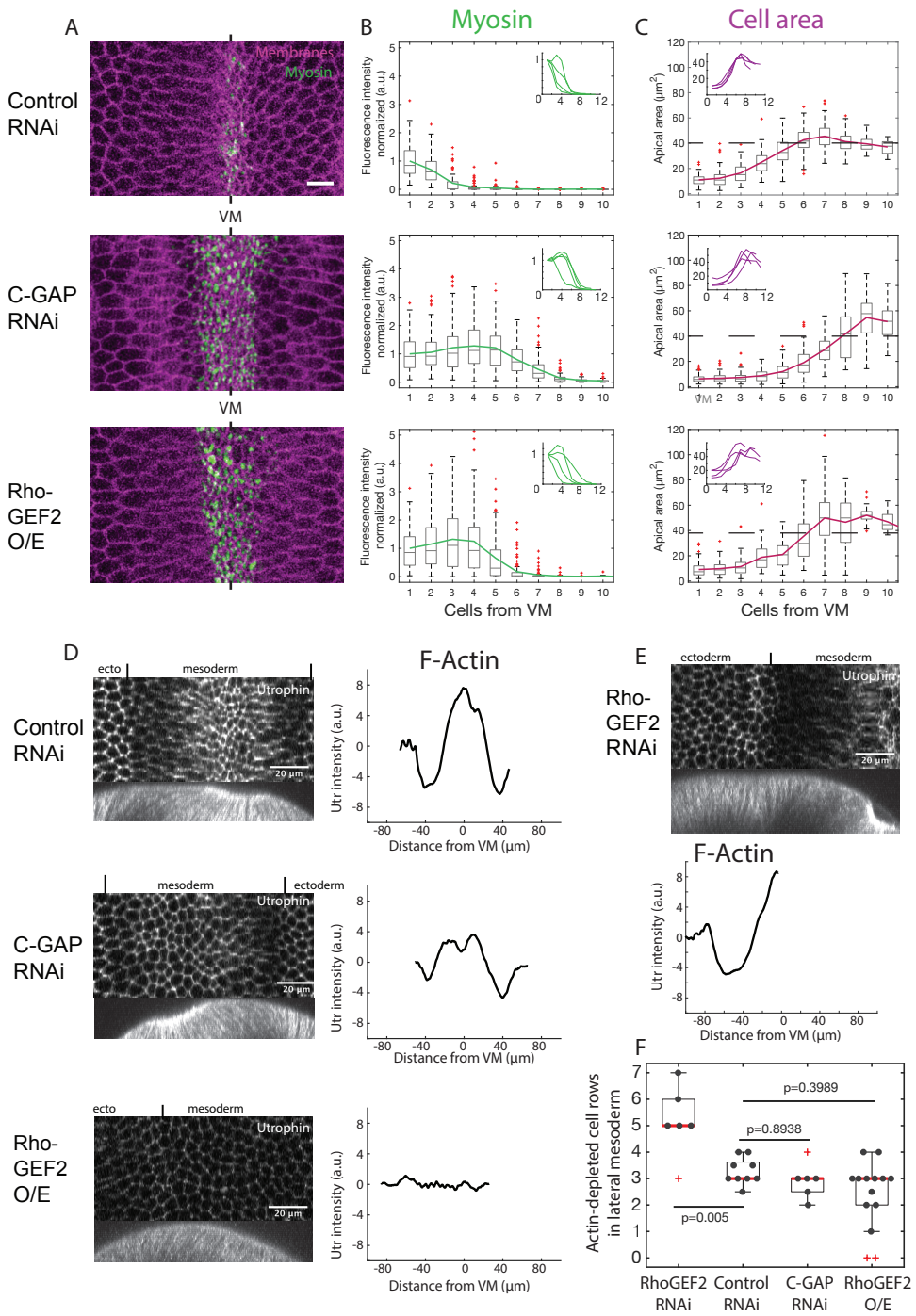

Figure 5: RhoA overactivation widens actomyosin gradient and narrows F-actin depleted zone. (**A**) Images (apical shell projections) of control (Rh3-RNAi), C-GAP-RNAi and RhoGEF2 O/E embryos expressing sqh::GFP (Myosin, green) and Gap43::mCherry (Membranes, magenta). Scale bar = 10 μm. (**B**) and (**C**) Quantification of normalized apical, active myosin (green, **B**) and apical area (magenta, **C**) as a function of distance from ventral

826 midline. Data is represented by box-and-whisker plot where each bin is a cell row at a given
827 distance from the ventral midline (at least 27 (control), 50 (C-GAP-RNAi) or 23 (RhoGEF2
828 O/E) cells per row analyzed, respectively; median 85 (control), 108.5 (C-GAP-RNAi) or 85
829 (RhoGEF2 O/E) cells). Bottom and top sides of the box represent 25th and 75th percentile,
830 respectively. Midline is the median and red points are outliers. Insets show 4 embryos for
831 each condition. (**D**) Width of F-actin depleted zone is narrower in C-GAP-RNAi and
832 RhoGEF2 O/E embryos. Left: Images (Top, subapical shell projection, and Bottom, 20 μm
833 maximum intensity projection of cross-section) of control (Rh3-RNAi), C-GAP-RNAi and
834 RhoGEF2 O/E embryos expressing Utrophin::GFP. Scale bars = 20 μm. Right:
835 Quantification of cortical F-actin levels by physical distance along the ventral-lateral axis.
836 Data is represented as mean intensity for one representative embryo. (**E**) Width of F-actin
837 depleted zone is wider in RhoGEF2-RNAi embryo. Top: Images (subapical shell projection
838 (top), and 20 μm maximum intensity projection of cross-section (below)) of RhoGEF2-RNAi
839 embryo expressing Utrophin::GFP. Scale bar = 20 μm. Bottom: Quantification of cortical F-
840 actin levels by physical distance along the ventral-lateral axis for one RhoGEF2-RNAi
841 embryo. (**F**) Width of F-actin depleted zone in cell rows for RhoGEF2-RNAi, control (Rh3-
842 RNAi), C-GAP-RNAi and RhoGEF2 O/E embryos. Data is represented by box-and-whisker
843 plot overlaid with data points for each analyzed embryo. Bottom and top sides of the box
844 represent 25th and 75th percentile, respectively. Midline is the median and red '+' are outliers.
845

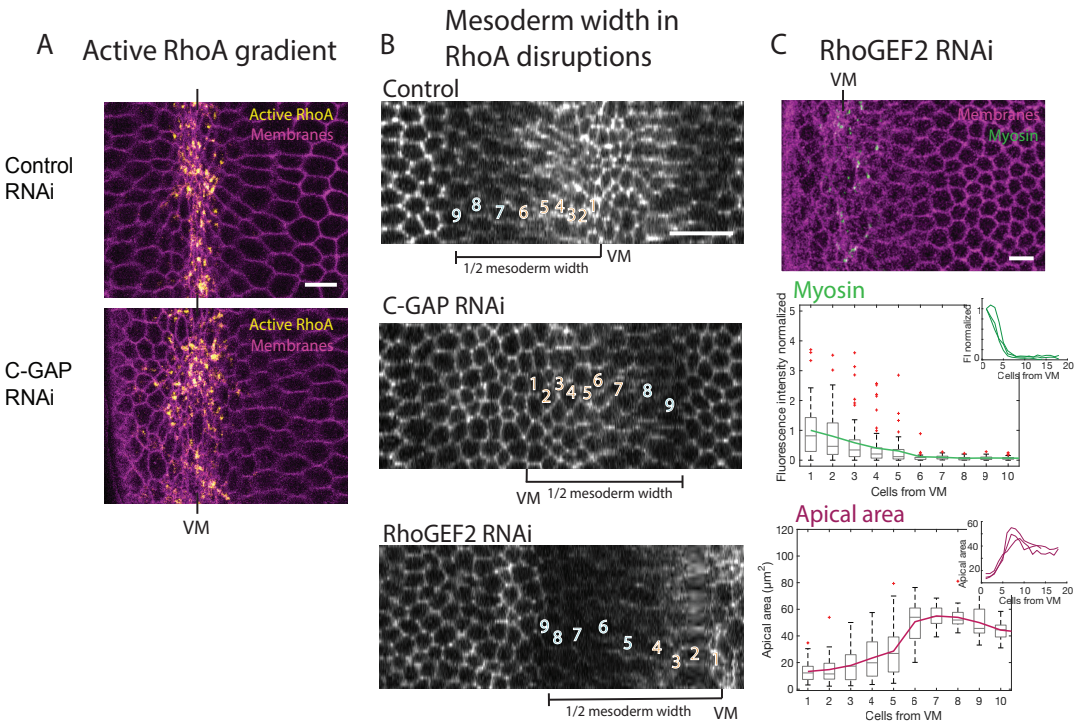

Supplement to Figure 5: RhoA and actomyosin gradient width, but not mesoderm width, are affected by RhoA regulators**.** (**A**) Images (apical shell projection) of control (Rh3-RNAi) and C-GAP-RNAi embryos expressing Anillin Rho-binding domain::GFP (active RhoA, yellow) and Gap43::mCherry (Membranes, magenta). Scale bar = 10 μm. (**B**) Subapical shell projections of embryos expressing Utrophin::GFP, indicating number of cell rows from the ventral midline to the mesoderm border (as visualized by change in F-actin level) for different genotypes (~9 cell rows). Cell rows with blue numbers are within the F-actin depleted zone and cell rows with orange numbers are within the F-actin gradient around the ventral midline. Scale bars = 20 μm. (**C**) Top: Image (apical shell projection) of RhoGEF2-RNAi embryo expressing sqh::GFP (Myosin, green) and Gap43::mCherry (Membranes, magenta). Scale bar = 10 μm. Bottom: Quantification of apical area (magenta) and normalized apical, active myosin (green) as a function of distance from ventral midline (at least 23 cells per cell row were analyzed; median 38 cells). Data is represented by box-and-whisker plot where each bin is a cell row at a given distance from the ventral midline. Bottom, and top, sides of the box represent 25th and 75th percentile of cells, respectively.

862 Midline is the median and red ‘+’ are outliers. Inset shows average cell behavior from 3

863 different embryos.

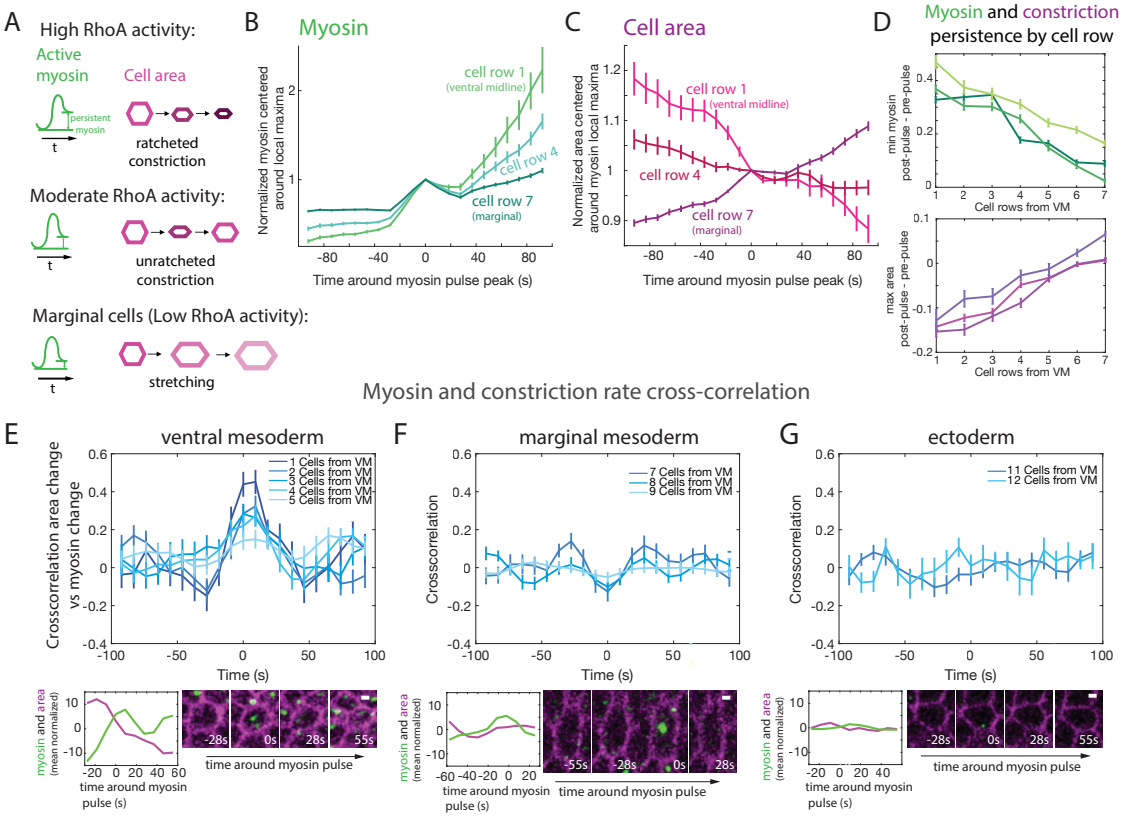

Figure 6: Contractile dynamics vary with ventral-lateral cell position. (**A**) There are distinct types of dynamic cell behaviors during ventral furrow formation. Top: When RhoA activity is high, cells preferably undergo “ratcheted” myosin pulses after which myosin increases and apical area is sustained. Middle: At moderate RhoA activity, cells undergo myosin pulses in which myosin and apical area reverse after contraction. Bottom: In marginal mesoderm cells, myosin pulses occur while the apical cell surface stretches, but the relationship of myosin and stretching dynamics was not understood. (**B**) Myosin persistence is highest close to the ventral midline. Average and standard error of myosin levels during and after a myosin pulse (local maxima in myosin accumulation rate) for cell row 1 at the midline (light green), intermediate cell row 4 (mint) and marginal mesoderm cell row 7 (dark green) shown for one representative embryo. 106 pulses were analyzed for cell row 1; 192 pulses were analyzed for cell row 4; 335 pulses were analyzed for cell row 7. (**C**) Myosin pulses away from the midline are associated with stretching. Average and standard error of apical area dynamics around pulses (local maxima in constriction rate) for cell row 1 at the midline (light magenta),

intermediate cell row 4 (maroon) and marginal mesoderm cell row 7 (dark magenta) shown for one representative embryo. 106 pulses were analyzed for cell row 1; 192 pulses were analyzed for cell row 4; 335 pulses were analyzed for cell row 7. (**D**) Average and standard error for persistence of myosin (minimum myosin 0-100 s after pulse - minimum myosin 0-100 s before pulse) and area (maximum area 0-100 s after pulse - maximum area 0-100 s before pulse) by bin (distance from the midline) for three embryos. At least 83 pulses were analyzed for each cell row in each embryo. Median 192, 238 and 343 pulses analyzed per cell row for the three embryos, respectively. (**E**)-(**F**) Top: Cross-correlation between the rate of change in apical myosin intensity (normalized to apical area) and constriction rate averaged by cell bin; split up by ventral mesoderm (cell rows 1-5, **E**), marginal mesoderm (cell rows 7-9, **F**) and ectoderm (cell rows 11 and 12, **G**). At least 21 cells per cell row were analyzed, median 32 cells per cell row. Bottom: Myosin (green) and apical area (magenta) traces (normalized to average) and images of representative individual cells during a myosin pulse, for each region. Scale bars = 2 μm.

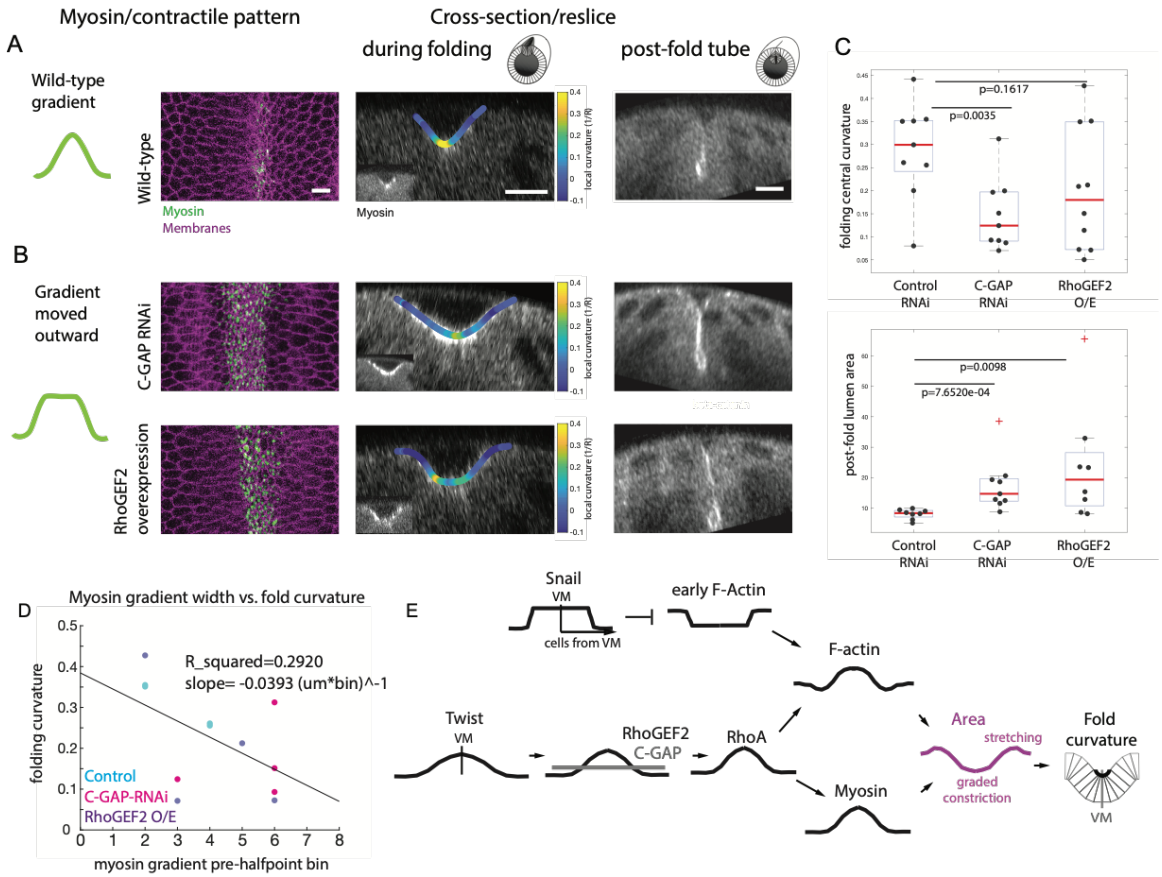

Figure 7: The contractile pattern determines fold curvature and post-fold shape. (**A**) Subapical shell projection and later cross-sections during and after folding of a single control (Rh3-RNAi) embryo expressing sqh::GFP (myosin) and gap43::mCh (membranes). In control embryos, in which the actomyosin gradient extends from cells 2-5, the ventral-lateral cross-section shows a narrow, v-shaped fold with high curvature at the center (local curvature is color-coded on the surface of the fold). The cross-sectional view of this embryo after folding shows a tube with a very small lumen. Scale bars = 10 μm. (**B**) Subapical shell projections and cross-sections during and after folding of a single C-GAP-RNAi embryo (top) and a single RhoGEF2 O/E embryo (bottom), expressing sqh::GFP (myosin) and gap43::mCh (membranes). C-GAP-RNAi and RhoGEF2 O/E embryos, which have a widened gradient with uniform myosin at the ventral midline display lower central fold curvature (local curvature is color-coded on the surface of the fold). At later timepoints, they often have an enlarged tube lumen as outlined by myosin signal in cross-section. (**C**)

909 Quantification of curvature at the center of the fold (measured by fitting a circle, 3
910 measurements at different AP positions averaged per embryo) (top) and lumen size
911 (measured by fitting an ellipse) (bottom) for control (Rh3-RNAi), C-GAP-RNAi and RhoGEF2
912 O/E embryos. Data is represented by box-and-whisker plot overlaid with data points
913 representing each quantified embryo. Bottom and top sides of the box represent 25th and
914 75th percentile of embryos, respectively. Midline is the median and red '+' are outliers. (**D**)
915 Regression analysis of the relationship between myosin gradient width and curvature for
916 control, C-GAP-RNAi and RhoGEF2 O/E embryos. Gradient width was measured as the cell
917 row bin that was just above the half-maximal intensity of the myosin gradient. Curvature was
918 measured as in (C). (**E**) Model for the regulation of tissue-wide patterning in the ventral
919 furrow. Uniform *snail* expression causes uniform F-actin depletion in the mesoderm. An
920 overlapping pattern of graded *twist* expression acts via tightly tuned RhoA activation to
921 generate an actomyosin gradient. Folding is driven by the combination of ventral midline cell
922 actomyosin contractility and stretching of marginal mesoderm cells, which are depleted of F-
923 actin.
924

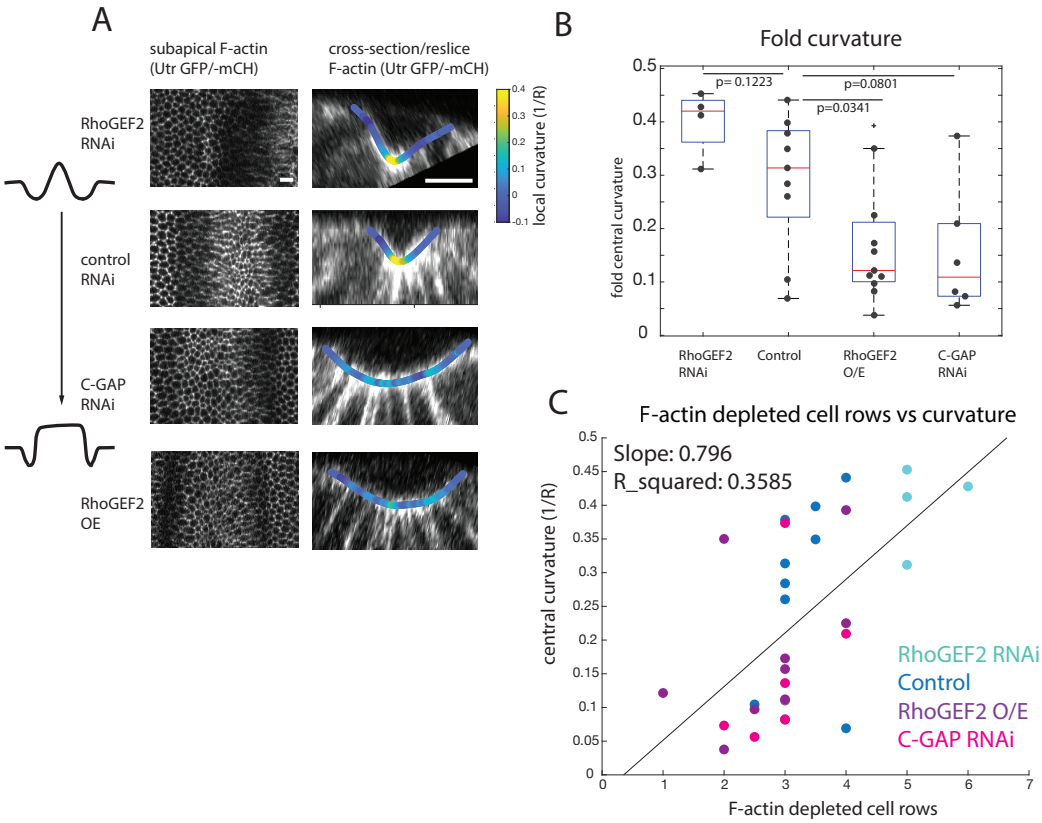

Supplement to Figure 7: The width of the F-actin depletion zone is correlated with fold curvature. (**A**) Subapical shell projections during early folding (left) and cross-sections (right) later during folding for single RhoGEF2-RNAi, control (Rh3-RNAi), C-GAP-RNAi and RhoGEF2 O/E embryos expressing Utrophin-GFP. In cross-section, local curvature is color-coded on the surface of the fold. Scale bars = 10 µm. (**B**) Quantification of curvature at the center of the fold (measured by fitting a circle, three measurements averaged per embryo) for RhoGEF2-RNAi, control (Rh3-RNAi), C-GAP-RNAi and RhoGEF2 O/E embryos. Data is represented by box-and-whisker plot overlaid with data points from all quantified embryos. Bottom, and top sides, of the box represent 25th and 75th percentile, respectively. Midline is the median and black '+' are outliers. (**C**) Regression analysis of the relationship between F-actin depleted region width and curvature for RhoGEF2-RNAi, control, C-GAP-RNAi and RhoGEF2 O/E embryos. Depleted F-actin region width was determined by the number of cell rows with low F-actin intensity. Curvature was measured as in (B).

Supplemental Movie S1 (related to Figure 4). Shell-projection (with background subtraction and gaussian blur) of control (Rh3-RNAi) embryo expressing sqh::GFP (myosin, green) and gap43::mCh (membranes, magenta) during ventral furrow formation. t=0 corresponds to the timepoint analyzed in Figure 4. Time step = 43.29 s, Frame rate = 2.5/s.

Supplemental Movie S2 (related to Figure 4). Shell-projection (with background subtraction and gaussian blur) of α-catenin-RNAi embryo expressing sqh::GFP (myosin, green) and gap43::mCh (membranes, magenta) trying to initiate ventral furrow formation. t=0 corresponds to the timepoint analyzed in Figure 4. Time step = 21.94 s, Frame rate = 5/s.

Supplemental Movie S3 (related to Figure 7). Maximum intensity projection of control (Rh3-RNAi) embryo expressing sqh::GFP (myosin, green) and gap43::mCh (membranes, magenta), during and after ventral furrow formation (gaussian blur radius =1). Time step = 53.653 s, Frame rate = 3.1/s.

Supplemental Movie S4 (related to Figure 7). Maximum intensity projection of RhoGEF2-RNAi embryo expressing sqh::GFP (myosin, green) and gap43::mCh (membranes, magenta), during and after ventral furrow formation (gaussian blur radius =1). Note divisions of mitotic domain 10 visible at the embryo surface after folding. Time step = 73.643 s, Frame rate = 4/s.

Supplemental table S1. Fly Stocks and crosses used in this study:

Stock	Genotype	Source/Reference	Figure
1	w; Gap43::mCherry(attp40); Sqh::GFP	Martin et al., 2010	
2	y, w[67c], sqh[AX3], cv; Sqh::GFP[42]	Bloomington Drosophila Stock Center	
3	OreR	Bloomington Drosophila Stock Center	1B-E, S1A, 2A
4	y[1] sc[*] v[1]; P{y[+t7.7] v[+t1.8]=TRiP.GL01052}attP2 (Rh3 shRNA control line)	Perkins et al., 2015	
5	w; mat67; mat15	Vasquez et al., 2014	
6	UtrABD-GFP;+	Rauzi et al. 2010	
7	w; gap43::mCherry/TM3, Sb[1]	Bardet et al. 2013	
8	Halo-sna/CyO-sqhGFP	Martin et al., 2009	
9	halo, twist[ey53] /CyO, Sqh::GFP	Martin et al., 2009	
10	UtrABD-mCH	Rauzi et al. 2010	
11	y w hs-flp; FRT42BG13 RhoGEF2[1.1]/CyO; GFP::Rhogef2 BAC(VK33)	Mason et al. 2016	
12	w[1118]; Df(2R)ED2747, P{w[+mW.Scer\FRT.hs3]=3'.RS5+3.3'}ED2747/SM6a; GFP::Rho	Mason et al. 2016	
13	Ubi-AniRBD-GFP; gap43mCH	This study (original Ubi>AniRBD-GFP stock: Munjal et al. 2015)	
14	Ubi-RokGFP; gap43mCh	Bardet et al. 2013	
15	w; mat67, Sqh::GFP; mat15, Gap43::mCherry/(TM3, Sb[1])	Vasquez et al., 2014	
16	Alpha-catenin RNAi (HMS), sqh-GFP	This study	
17	Alpha-catenin RNAi (HMS)	Perkins et al., 2015	
18	sqhGFP; P{y[+t7.7] v[+t1.8]=TRiP.GL01052}attP2 (Rh3 shRNA control line)	this study	
19	sqhGFP; P{TRiP.HMS00412}attP2 (RhoGAP71E, C-GAP shRNA)	This study	
20	y[1] w[*]; P{UASp-T7.RhoGEF2}5 (RhoGEF2 overexpression line)	Bloomington Drosophila Stock Center	
21	y,w; Sqh::GFP; mat15, Gap43::mCherry/(TM3, Sb[1])	Vasquez et al., 2014	
22	y[1] sc[*] v[1]; P{TRiP.HMS00412}attP2 (*RhoGAP71E, C-GAP shRNA*)	Perkins et al., 2015	
23	Mat 67, UtrABD-GFP	Jodoin and Martin, 2016	
24	mat15, Utr::GFP; sqhmCH	This study	
25	mat15, Utr::mCh	This study	
26	y[1] sc[*] v[1]; P{TRiP.HMS01118}attP2 (*RhoGEF2 shRNA*)	Perkins et al., 2015	
27	Ubi-AniRBD-GFP; 71E HMS	This study	
28	Ubi-AniRBD-GFP; RH3GL	this study	
29	mat67; mat15, gap43::mCh	Vasquez et al., 2014	
30	y,w;+;C-GAP-GFP	This study	1B, S3A
	F2 embryos imaged from these crosses, using above stock numbers/genotypes. Non-balancer females were used for cages.		
	Stock # 1 x 2 (Virgins x males)		1A, 6
	4x5		4D, S4A
	6x7		S1
	8x6		2B,C
	8x10		2B, C
	8x6		2D,E
	9x10		2D,E
	11x12		3B,C
	13x3		3D, E
	14x3		3F,G
	4x15		4A-C,E, 5A-C, 7A,C,D
	18x15		4A-C,E, 5A-C, 6B-G
	16x15		4A-C,E
	17x5		4D-E, S4B
	4x21		5A-C, 7B-D
	19x15		5A-C, S6A,B, 7B-D
	20x21	cages kept at RT >24h before imaging	5A-C, 7B-D
	4x23		5D,F, S5C, S7A-C
	22x23		5D,F, S5C, S7A-C
	20x24	cages kept at RT >24h before imaging	5D,F, S7A-C
	20x23	cages kept at RT >24h before imaging	5D,F, S7A-C
	20x25	cages kept at RT >24h before imaging	5D,F, S7A-C
	26x23	cages kept at RT >24h before imaging	5E,F, S5C, S7A-C
	27x29		S5A
	28x29		S5A
	26x 21	cages kept at RT >24h before imaging	S5B

References:

Bardet, P. L., B. Guirao, C. Paoletti, F. Serman, V. Léopold, F. Bosveld, Y. Goya, V. Mirouse, F. Graner, and Y. Bellaïche. 2013. PTEN controls junction lengthening and stability during cell rearrangement in epithelial tissue. *Dev. Cell*. 25:534–546.

Chanet, S., Miller, C. J., Vaishnav, E. D., Ermentrout, B., Davidson, L. A., & Martin, A. C. (2017). Actomyosin meshwork mechanosensing enables tissue shape to orient cell force. *Nature Communications*, *8*, 15014. https://doi.org/10.1038/ncomms15014

Jodoin, J. N., & Martin, A. C. (2016). Abl suppresses cell extrusion and intercalation during epithelium folding. *Molecular Biology of the Cell*, *27* (18), 2822–2832. https://doi.org/10.1091/mbc.E16-05-0336

Martin, A.C., M. Gelbart, R. Fernandez-Gonzalez, M. Kaschube, and E.F. Wieschaus. 2010. Integration of contractile forces during tissue invagination. *J. Cell Biol.* 188:735–749.

Martin, A.C., M. Kaschube, and E.F. Wieschaus. 2009. Pulsed contractions of an actin-myosin network drive apical constriction. *Nature*. 457:495–499.

Mason, F. M., Xie, S., Vasquez, C. G., Tworoger, M., & Martin, A. C. (2016). RhoA GTPase inhibition organizes contraction during epithelial morphogenesis. *The Journal of Cell Biology*, *214* (5). Retrieved from http://jcb.rupress.org/content/214/5/603.long

Munjal, A., J.-M. Philippe, E. Munro, and T. Lecuit. 2015. A self-organized biomechanical network drives shape changes during tissue morphogenesis. *Nature*. 524:351–355.

Perkins, L. A., L. Holderbaum, R. Tao, Y. Hu, R. Sopko, K. McCall, D. Yang-Zhou, I. Flockhart, R. Binari, H.-S. Shim, et al. 2015. The Transgenic RNAi Project at Harvard Medical School: resources and validation. *Genetics*. 201:843–852.

Rauzi, M., Lenne, P. F., & Lecuit, T. (2010). Planar polarized actomyosin contractile flows control epithelial junction remodelling. *Nature*. https://doi.org/10.1038/nature09566

Vasquez, C.G., M. Tworoger, and A.C. Martin. 2014. Dynamic myosin phosphorylation regulates contractile pulses and tissue integrity during epithelial morphogenesis. *J. Cell Biol.* 206:435–450.

Supplemental Table S2. Imaging settings used in this study:

Imaging settings

Fluorescent tag combination	Figures	Excitation laser wavelength	Detector start wavelength (nm)	Detector end wavelength (nm)	Detector Gain (a.u.)	Laser power (%)	Pinhole size (x10^(-4) m)
sqh::GFP (Myosin)	1A, 4A-C, S4C, 5A, S5b, 6, S6, 7	488	493	537.57 to 586	700 to 874.081	2 to 7	76.545 to 89.944
gap43mCh (Membranes)	1A, S1B, 3, S3, 4A-C, S4C, 5A, S5A+B, 6, S6, 7	561	569.57 to 603.82	696 to 698.26	763 to 866	2 to 6.5	76.545 to 89.944
		594	600.32 to 614.82	696	840-856	5-6.5	
Utrophin::GFP	S1B, 2B,C, 5D-F, S5C, S7	488	493	562.07 to 598	770-850	2 to 4	89.944
Utrophin::mCh	2B-E, 5D-F, S7	561	578	696	770-800	4.3 to 5	89.944
RhoGEF2::GFP	3B	488	493	561	850	12	89.944
Anillin::GFP+[Imagingsettings.:	3C	488	493	561	850	12 to 22	89.944
Rok-GFP	3D	488	493	561	850	7	89.944
C-GAP-GFP	S3	488	493	565	900	16	89.214
Phalloidin Alexa Fluor 568	1B-D, S1A, 4D, S4A, B	561	569 to 574	647 to 712	600 to 700	1 to 2	37.175 to 77.853
Alexa Fluor 488 secondary antibody	S1A (snail), 2A (snail), S4A (armadillo)	488	493	574	500-600	2	45.511 or 89.213
Alexa Fluor 647 secondary antibody	S4A (ecadherin)	633	647	755	800	5	42.175
Alexa Fluor 568 secondary antibody	S4A (Snail)	568	574	712	600	1.2	89.213
sqhGFP fixed	S4A	488	493	569	800	8	37.175

970

971 **References**

972

973 Bailles, A., C. Collinet, J.M. Philippe, P.F. Lenne, E. Munro, and T. Lecuit. 2019. Genetic
974 induction and mechanochemical propagation of a morphogenetic wave. *Nature*.
975 572:467-473.
976 Barrett, K., M. Leptin, and J. Settleman. 1997. The Rho GTPase and a putative RhoGEF
977 mediate a signaling pathway for the cell shape changes in Drosophila gastrulation.
978 *Cell*. 91:905-915.
979 Boulay, J.L., C. Dennefeld, and A. Alberga. 1987. The Drosophila developmental gene snail
980 encodes a protein with nucleic acid binding fingers. *Nature*. 330:395-398.
981 Chanet, S., C.J. Miller, E.D. Vaishnav, B. Ermentrout, L.A. Davidson, and A.C. Martin.
982 2017. Actomyosin meshwork mechanosensing enables tissue shape to orient cell
983 force. *Nat Commun*. 8:15014.
984 Chanet, S., and F. Schweisguth. 2012. Regulation of epithelial polarity by the E3 ubiquitin
985 ligase Neuralized and the Bearded inhibitors in Drosophila. *Nat Cell Biol*. 14:467-
986 476.
987 Costa, M., E.T. Wilson, and E. Wieschaus. 1994. A putative cell signal encoded by the folded
988 gastrulation gene coordinates cell shape changes during Drosophila gastrulation. *Cell*.
989 76:1075-1089.
990 Dawes-Hoang, R.E., K.M. Parmar, A.E. Christiansen, C.B. Phelps, A.H. Brand, and E.F.
991 Wieschaus. 2005. folded gastrulation, cell shape change and the control of myosin
992 localization. *Development*. 132:4165-4178.
993 Denk-Lobnig, M., and A.C. Martin. 2019. Modular regulation of Rho family GTPases in
994 development. *Small GTPases*. 10:122-129.
995 Fernandez-Gonzalez, R., and J.A. Zallen. 2011. Oscillatory behaviors and hierarchical
996 assembly of contractile structures in intercalating cells. *Phys Biol*. 8:045005.
997 Foe, V.E. 1989. Mitotic domains reveal early commitment of cells in Drosophila embryos.
998 *Development*. 107:1-22.
999 Fox, D.T., and M. Peifer. 2007. Abelson kinase (Abl) and RhoGEF2 regulate actin
1000 organization during cell constriction in Drosophila. *Development*. 134:567-578.
1001 Furlong, E.E., E.C. Andersen, B. Null, K.P. White, and M.P. Scott. 2001. Patterns of gene
1002 expression during Drosophila mesoderm development. *Science*. 293:1629-1633.
1003 Fuse, N., F. Yu, and S. Hirose. 2013. Gprk2 adjusts Fog signaling to organize cell
1004 movements in Drosophila gastrulation. *Development*. 140:4246-4255.
1005 Gelbart, M.A., B. He, A.C. Martin, S.Y. Thiberge, E.F. Wieschaus, and M. Kaschube. 2012.
1006 Volume conservation principle involved in cell lengthening and nucleus movement
1007 during tissue morphogenesis. *Proc Natl Acad Sci U S A*. 109:19298-19303.
1008 Gratz, S.J., M.M. Harrison, J. Wildonger, and K.M. O'Connor-Giles. 2015. Precise Genome
1009 Editing of Drosophila with CRISPR RNA-Guided Cas9. *Methods Mol Biol*.
1010 1311:335-348.
1011 Gratz, S.J., F.P. Ukken, C.D. Rubinstein, G. Thiede, L.K. Donohue, A.M. Cummings, and
1012 K.M. O'Connor-Giles. 2014. Highly specific and efficient CRISPR/Cas9-catalyzed
1013 homology-directed repair in Drosophila. *Genetics*. 196:961-971.
1014 Grosshans, J., and E. Wieschaus. 2000. A genetic link between morphogenesis and cell
1015 division during formation of the ventral furrow in Drosophila. *Cell*. 101:523-531.
1016 Hacker, U., and N. Perrimon. 1998. DRhoGEF2 encodes a member of the Dbl family of
1017 oncogenes and controls cell shape changes during gastrulation in Drosophila. *Genes*
1018 *Dev*. 12:274-284.

1019 Heer, N.C., P.W. Miller, S. Chanet, N. Stoop, J. Dunkel, and A.C. Martin. 2017.
1020 Actomyosin-based tissue folding requires a multicellular myosin gradient.
1021 *Development*. 144:1876-1886.
1022 Homem, C.C., and M. Peifer. 2008. Diaphanous regulates myosin and adherens junctions to
1023 control cell contractility and protrusive behavior during morphogenesis. *Development*.
1024 135:1005-1018.
1025 Hong, L., M. Dumond, S. Tsugawa, A. Sapala, A.L. Routier-Kierzkowska, Y. Zhou, C. Chen,
1026 A. Kiss, M. Zhu, O. Hamant, R.S. Smith, T. Komatsuzaki, C.B. Li, A. Boudaoud, and
1027 A.H. Roeder. 2016. Variable Cell Growth Yields Reproducible OrganDevelopment
1028 through Spatiotemporal Averaging. *Dev Cell*. 38:15-32.
1029 Iseli, C., G. Ambrosini, P. Bucher, and C.V. Jongeneel. 2007. Indexing strategies for rapid
1030 searches of short words in genome sequences. *PLoS One*. 2:e579.
1031 Jha, A., T.S. van Zanten, J.M. Philippe, S. Mayor, and T. Lecuit. 2018. Quantitative Control
1032 of GPCR Organization and Signaling by Endocytosis in Epithelial Morphogenesis.
1033 *Curr Biol*. 28:1570-1584 e1576.
1034 Jodoin, J.N., J.S. Coravos, S. Chanet, C.G. Vasquez, M. Tworoger, E.R. Kingston, L.A.
1035 Perkins, N. Perrimon, and A.C. Martin. 2015. Stable Force Balance between
1036 Epithelial Cells Arises from F-Actin Turnover. *Dev Cell*. 35:685-697.
1037 Kerridge, S., A. Munjal, J.M. Philippe, A. Jha, A.G. de las Bayonas, A.J. Saurin, and T.
1038 Lecuit. 2016. Modular activation of Rho1 by GPCR signalling imparts polarized
1039 myosin II activation during morphogenesis. *Nat Cell Biol*. 18:261-270.
1040 Ko, C.S., P. Kalakuntla, and A.C. Martin. 2020. Apical Constriction Reversal upon Mitotic
1041 Entry Underlies Different Morphogenetic Outcomes of Cell Division. *Mol Biol*
1042 *Cell*:mbcE19120673.
1043 Kolsch, V., T. Seher, G.J. Fernandez-Ballester, L. Serrano, and M. Leptin. 2007. Control of
1044 Drosophila gastrulation by apical localization of adherens junctions and RhoGEF2.
1045 *Science*. 315:384-386.
1046 Latorre, E., S. Kale, L. Casares, M. Gomez-Gonzalez, M. Uroz, L. Valon, R.V. Nair, E.
1047 Garreta, N. Montserrat, A. Del Campo, B. Ladoux, M. Arroyo, and X. Trepat. 2018.
1048 Active superelasticity in three-dimensional epithelia of controlled shape. *Nature*.
1049 563:203-208.
1050 Leptin, M. 1991. twist and snail as positive and negative regulators during Drosophila
1051 mesoderm development. *Genes Dev*. 5:1568-1576.
1052 Leptin, M. 2005. Gastrulation movements: the logic and the nuts and bolts. *Dev Cell*. 8:305-
1053 320.
1054 Leptin, M., and B. Grunewald. 1990. Cell shape changes during gastrulation in Drosophila.
1055 *Development*. 110:73-84.
1056 Lim, B., M. Levine, and Y. Yamazaki. 2017. Transcriptional Pre-patterning of Drosophila
1057 Gastrulation. *Curr Biol*. 27:610.
1058 Manning, A.J., K.A. Peters, M. Peifer, and S.L. Rogers. 2013. Regulation of epithelial
1059 morphogenesis by the G protein-coupled receptor mist and its ligand fog. *Sci Signal*.
1060 6:ra98.
1061 Martin, A.C., M. Gelbart, R. Fernandez-Gonzalez, M. Kaschube, and E.F. Wieschaus. 2010.
1062 Integration of contractile forces during tissue invagination. *J Cell Biol*. 188:735-749.
1063 Martin, A.C., M. Kaschube, and E.F. Wieschaus. 2009. Pulsed contractions of an actin-
1064 myosin network drive apical constriction. *Nature*. 457:495-499.
1065 Mason, F.M., M. Tworoger, and A.C. Martin. 2013. Apical domain polarization localizes
1066 actin-myosin activity to drive ratchet-like apical constriction. *Nat Cell Biol*. 15:926-
1067 936.

1068 Mason, F.M., S. Xie, C.G. Vasquez, M. Tworoger, and A.C. Martin. 2016. RhoA GTPase
1069 inhibition organizes contraction during epithelial morphogenesis. *J Cell Biol*.
1070 214:603-617.
1071 Mitrossilis, D., J.C. Roper, D. Le Roy, B. Driquez, A. Michel, C. Menager, G. Shaw, S. Le
1072 Denmat, L. Ranno, F. Dumas-Bouchiat, N.M. Dempsey, and E. Farge. 2017.
1073 Mechanotransductive cascade of Myo-II-dependent mesoderm and endoderm
1074 invaginations in embryo gastrulation. *Nat Commun*. 8:13883.
1075 Mongera, A., P. Rowghanian, H.J. Gustafson, E. Shelton, D.A. Kealhofer, E.K. Carn, F.
1076 Serwane, A.A. Lucio, J. Giammona, and O. Campas. 2018. A fluid-to-solid jamming
1077 transition underlies vertebrate body axis elongation. *Nature*. 561:401-405.
1078 Munjal, A., J.M. Philippe, E. Munro, and T. Lecuit. 2015. A self-organized biomechanical
1079 network drives shape changes during tissue morphogenesis. *Nature*. 524:351-355.
1080 Nikolaidou, K.K., and K. Barrett. 2004. A Rho GTPase signaling pathway is used
1081 reiteratively in epithelial folding and potentially selects the outcome of Rho
1082 activation. *Curr Biol*. 14:1822-1826.
1083 Perez-Mockus, G., K. Mazouni, V. Roca, G. Corradi, V. Conte, and F. Schweisguth. 2017.
1084 Spatial regulation of contractility by Neuralized and Bearded during furrow
1085 invagination in Drosophila. *Nat Commun*. 8:1594.
1086 Rahimi, N., I. Averbukh, S. Carmon, E.D. Schejter, N. Barkai, and B.Z. Shilo. 2019.
1087 Dynamics of Spaetzle morphogen shuttling in the Drosophila embryo shapes pattern.
1088 *Development*. 146:doi: 10.1242/dev.181487.
1089 Rauzi, M., U. Krzic, T.E. Saunders, M. Krajnc, P. Ziherl, L. Hufnagel, and M. Leptin. 2015.
1090 Embryo-scale tissue mechanics during Drosophila gastrulation movements. *Nat*
1091 *Commun*. 6:8677.
1092 Rembold, M., L. Ciglar, J.O. Yanez-Cuna, R.P. Zinzen, C. Girardot, A. Jain, M.A. Welte, A.
1093 Stark, M. Leptin, and E.E. Furlong. 2014. A conserved role for Snail as a potentiator
1094 of active transcription. *Genes Dev*. 28:167-181.
1095 Rogers, K.W., and A.F. Schier. 2011. Morphogen gradients: from generation to
1096 interpretation. *Annu Rev Cell Dev Biol*. 27:377-407.
1097 Salbreux, G., G. Charras, and E. Paluch. 2012. Actin cortex mechanics and cellular
1098 morphogenesis. *Trends Cell Biol*. 22:536-545.
1099 Schindelin, J., I. Arganda-Carreras, E. Frise, V. Kaynig, M. Longair, T. Pietzsch, S.
1100 Preibisch, C. Rueden, S. Saalfeld, B. Schmid, J.Y. Tinevez, D.J. White, V.
1101 Hartenstein, K. Eliceiri, P. Tomancak, and A. Cardona. 2012. Fiji: an open-source
1102 platform for biological-image analysis. *Nat Methods*. 9:676-682.
1103 Spahn, P., and R. Reuter. 2013. A vertex model of Drosophila ventral furrow formation.
1104 *PLoS One*. 8:e75051.
1105 Spracklen, A.J., T.N. Fagan, K.E. Lovander, and T.L. Tootle. 2014. The pros and cons of
1106 common actin labeling tools for visualizing actin dynamics during Drosophila
1107 oogenesis. *Dev Biol*. 393:209-226.
1108 Stricker, J., T. Falzone, and M.L. Gardel. 2010. Mechanics of the F-actin cytoskeleton. *J*
1109 *Biomech*. 43:9-14.
1110 Sui, L., S. Alt, M. Weigert, N. Dye, S. Eaton, F. Jug, E.W. Myers, F. Julicher, G. Salbreux,
1111 and C. Dahmann. 2018. Differential lateral and basal tension drive folding of
1112 Drosophila wing discs through two distinct mechanisms. *Nat Commun*. 9:4620.
1113 Sumigray, K.D., M. Terwilliger, and T. Lechler. 2018. Morphogenesis and
1114 Compartmentalization of the Intestinal Crypt. *Dev Cell*. 45:183-197 e185.
1115 Sweeton, D., S. Parks, M. Costa, and E. Wieschaus. 1991. Gastrulation in Drosophila: the
1116 formation of the ventral furrow and posterior midgut invaginations. *Development*.
1117 112:775-789.

1118 Thisse, B., C. Stoetzel, C. Gorostiza-Thisse, and F. Perrin-Schmitt. 1988. Sequence of the
1119 twist gene and nuclear localization of its protein in endomesodermal cells of early
1120 Drosophila embryos. *EMBO J*. 7:2175-2183.
1121 Ulrich, A., K.R. Andersen, and T.U. Schwartz. 2012. Exponential megapriming PCR (EMP)
1122 cloning--seamless DNA insertion into any target plasmid without sequence
1123 constraints. *PLoS One*. 7:e53360.
1124 Vasquez, C.G., M. Tworoger, and A.C. Martin. 2014. Dynamic myosin phosphorylation
1125 regulates contractile pulses and tissue integrity during epithelial morphogenesis. *J*
1126 *Cell Biol*. 206:435-450.
1127 von Dassow, M., and L.A. Davidson. 2009. Natural variation in embryo mechanics:
1128 gastrulation in Xenopus laevis is highly robust to variation in tissue stiffness. *Dev*
1129 *Dyn*. 238:2-18.
1130 Weng, M., and E. Wieschaus. 2016. Myosin-dependent remodeling of adherens junctions
1131 protects junctions from Snail-dependent disassembly. *J Cell Biol*. 212:219-229.
1132 Wolpert, L. 1969. Positional information and the spatial pattern of cellular differentiation. *J*
1133 *Theor Biol*. 25:1-47.
1134 Xie, S., and A.C. Martin. 2015. Intracellular signalling and intercellular coupling coordinate
1135 heterogeneous contractile events to facilitate tissue folding. *Nat Commun*. 6:7161.
1136 Yevick, H.G., P.W. Miller, J. Dunkel, and A.C. Martin. 2019. Structural Redundancy in
1137 Supracellular Actomyosin Networks Enables Robust Tissue Folding. *Dev Cell*.
1138 50:586-598.

1139

1140